

Novel Tornado-Like Vortex Generator with Intelligent Controller

by

Xin Liu

A thesis
presented to the University of Waterloo
in fulfillment of the
thesis requirement for the degree of
Master of Applied Science
in
Mechanical and Mechatronics Engineering

Waterloo, Ontario, Canada, 2021

© Xin Liu 2021

Author's Declaration

I hereby declare that I am the sole author of this thesis. This is a true copy of the thesis, including any required final revisions, as accepted by my examiners.

I understand that my thesis may be made electronically available to the public.

Abstract

Cooking fumes may cause multiple adverse health effects, and range hoods play central roles in controlling indoor air pollution caused by cooking fumes. However, the traditional design of the range hoods has a low efficiency due to its working principle, and the efficiency decreases rapidly as the mounting height of the exhaust hood increases.

This thesis is aimed at design and building a novel tornado-like vortex generator (TLVG) with an intelligent controller to enhance the efficiency of traditional range hood. Both experimental results and numerical simulation indicate that most of the cooking fumes are spreading to surrounding areas when the traditional range hood is working alone, while the cooking fumes are drawn into the tornado-like vortex and exhausted through the range hood when the novel TLVG is on.

The effects of various factors on the efficiency of sucking cooking fumes are analyzed by orthogonal experiment design. The results show that the key factor affecting the performance of the TLVG is the horizontal jet angle. A higher jet velocity results in a lower negative pressure, which helps concentrate and exhaust the fume. The results also reveal that the exhaust flow velocity marginally affects the pressure around the source of cooking fumes, but the tornado-like vortex cannot be produced when the value of the exhaust flow velocity is too high. In addition, the figures of the velocity field, pressure field, and tracking particle field are plotted and analyzed.

In this thesis, an intelligent controller of TLVG is designed and simulated to adapt to various types of range hoods. Adaptive-Network-based Fuzzy Inference System (ANFIS) is used in this intelligent controller, which combines the merits of both Fuzzy Inference Systems and Neural Networks. The results from the numerical simulation of the TLVG can be used to train and test the neural fuzzy system. Besides, Particle Swarm Optimization (PSO) is used for effective training in ANFIS networks. Digital simulation results demonstrate that the designed ANFIS-Swarm controller realizes a better prediction of the checking data than that from a basic ANFIS controller.

This study provides information for improving the kitchen environment, and it can also be applied to different types of range hood, exhaust ventilation system, and air pollution control.

Acknowledgements

Firstly, I would like to take this opportunity to express special thanks to my supervisors, Professor Fue-Sang Lien and William Melek for their invaluable support and guidance in this master research project. Prof. Melek gave me guidance of control theory and artificial intelligence, and Prof. Lien helped me a lot from the knowledge of CFD to the lessons of life. I know I would never have made it this far without their help and support.

Also, I would like to thank Jason Benninger for building the experimental device. Jason has extensive experience in this area, and he is always willing to teach me and provide me with advice. Without his help, this study could hardly proceed.

Besides, I would like to thank Natural Sciences and Engineering Research Council (NSERC) of Canada and Ontario Centres of Excellence (OCE) for supporting and funding this project. Besides, many thanks to my lab mates for constructive suggestions. Thanks to the University of Waterloo as well. Lastly, I want to thank my family. Their support and love keep me going in my career.

Table of Contents

| | |
|---|----------|
| List of Tables | viii |
| List of Figures | ix |
| 1 Introduction | 1 |
| 1.1 Motivation | 1 |
| 1.2 Objectives | 2 |
| 1.3 Contributions | 3 |
| 1.4 Thesis Organization | 4 |
| 2 Background and Literature Review | 5 |
| 2.1 Computational Method | 5 |
| 2.1.1 Governing Equations | 5 |
| 2.1.2 Turbulence Modelling | 6 |
| 2.1.3 DPM | 7 |
| 2.2 Control Theory | 8 |
| 2.2.1 Fuzzy System | 8 |
| 2.2.2 ANFIS | 10 |
| 2.2.3 PSO | 12 |

| | | |
|----------|---|-----------|
| 3 | Methodology | 15 |
| 3.1 | Experimental Setup | 15 |
| 3.2 | Numerical Modelling | 18 |
| 3.2.1 | Domain and Setups | 18 |
| 3.2.2 | Boundary Conditions | 19 |
| 3.2.3 | Mesh Independence Test | 23 |
| 3.3 | Design of Orthogonal Experiment | 24 |
| 3.4 | Controller | 31 |
| 3.4.1 | Design of the Intelligent Controller | 31 |
| 3.4.2 | Training Data | 33 |
| 3.4.3 | ANFIS with PSO | 34 |
| 4 | Result and Discussion | 36 |
| 4.1 | Comparison between Experiment and Simulation | 36 |
| 4.2 | Results of Orthogonal Experimental Design | 39 |
| 4.3 | Effects of Different Factors on Tornado-Like Vertex | 41 |
| 4.3.1 | Jet Velocity | 41 |
| 4.3.2 | Range Hood Exhaust Flow Velocity | 43 |
| 4.4 | Interaction between Two Tornado-like vortices | 45 |
| 4.5 | Side-Suction Range Hood | 47 |
| 4.6 | Intelligent Controller of TLVG | 51 |
| 4.6.1 | Results of Standard ANFIS | 51 |
| 4.6.2 | Results of ANFIS with PSO | 54 |
| 5 | Conclusion and Future Works | 56 |
| 5.1 | Conclusion | 56 |
| 5.2 | Future Work | 57 |
| | References | 59 |

| | |
|--------------------------------|-----------|
| APPENDICES | 63 |
| A Orthogonal Table | 64 |
| B PDF Plots From Matlab | 67 |

List of Tables

| | | |
|-----|--|----|
| 1.1 | Parameters of different range hoods. | 2 |
| 3.1 | Jet velocities at the measuring point vs the jet velocities. | 21 |
| 3.2 | Five mesh levels and corresponding properties. | 23 |
| 3.3 | Factors and levels of orthogonal experimental design. | 28 |
| 3.4 | $L_{18}(3^5)$ orthogonal experimental plan layout. | 29 |
| 3.5 | Parameters of PSO. | 34 |
| 4.1 | Results of orthogonal experiment. | 40 |
| 4.2 | Extreme difference analysis of orthogonal experiment. | 41 |
| 4.3 | Percentage of exhausted particles for different jet velocities. | 42 |
| 4.4 | Percentage of exhausted particles for different exhaust flow velocities. | 44 |
| 4.5 | Percentage of exhausted particles for 4 cases | 47 |
| A.1 | $L_9(3^4)$ orthogonal table. | 65 |
| A.2 | $L_{18}(3^5)$ orthogonal table. | 66 |

List of Figures

| | | |
|------|---|----|
| 2.1 | Fuzzy inference system. | 9 |
| 2.2 | ANFIS network architecture. | 10 |
| 2.3 | Two pass hybrid learning algorithm for ANFIS. | 11 |
| 2.4 | Steps in the PSO algorithm. | 13 |
| 2.5 | Concept of modification of a searching point by PSO. | 14 |
| 3.1 | The frame of TLVG device. | 16 |
| 3.2 | Two types of range hoods. | 16 |
| 3.3 | Vertical slide guides and lock mechanisms. | 17 |
| 3.4 | Schematic diagram of the tubes. | 17 |
| 3.5 | DC fan at end of tube. | 18 |
| 3.6 | The mist maker. | 18 |
| 3.7 | The experimental device of the TLVG. | 19 |
| 3.8 | The 3D model of the TLVG. | 20 |
| 3.9 | The hand-held digital anemometer. | 21 |
| 3.10 | Velocities on the horizontal line from the hole to the measure point. | 22 |
| 3.11 | Tetrahedral mesh on the surface of the domain. | 24 |
| 3.12 | Mesh refinement at the hole on the surface of the tube. | 24 |
| 3.13 | The planes of cross section, central line and horizontal line of the model. | 25 |
| 3.14 | The static pressure on the vertical central line. | 25 |
| 3.15 | The velocity magnitude on the vertical central line. | 26 |

| | | |
|------|---|----|
| 3.16 | Five factors in orthogonal experimental design and the pressure monitoring point. | 27 |
| 3.17 | ANFIS Architecture. | 32 |
| 3.18 | ANFIS training data. | 34 |
| 4.1 | Mist distribution comparison. | 37 |
| 4.2 | Particle tracking comparison. | 38 |
| 4.3 | Static pressure comparison. | 38 |
| 4.4 | The static pressure on the central line. | 39 |
| 4.5 | Pressure on the central line with different jet velocities. | 42 |
| 4.6 | Velocity vector on the horizontal cross plane with different jet velocities. | 43 |
| 4.7 | Pressure on the central line with different exhaust flow velocities. | 44 |
| 4.8 | Pressure contour on the vertical cross plane with different jet velocities. | 45 |
| 4.9 | Velocity vector on the horizontal cross plane. | 46 |
| 4.10 | Pressure contour on the vertical cross plane. | 48 |
| 4.11 | Mist distribution comparison in the experiment. | 49 |
| 4.12 | The side-suction range hood. | 50 |
| 4.13 | Pressure on the vertical plane with side-suction range hood. | 50 |
| 4.14 | Pathline of jet flow with side-suction range hood. | 51 |
| 4.15 | Matlab ANFIS Architecture. | 52 |
| 4.16 | Membership Functions of inputs for basic ANFIS. | 52 |
| 4.17 | Relationship Between Two Inputs and One Output. | 53 |
| 4.18 | Checking Data and System Outputs for standard ANFIS. | 53 |
| 4.19 | Membership Functions of inputs for ANFIS with PSO. | 54 |
| 4.20 | Checking Data and System Outputs for ANFIS with PSO. | 55 |
| 5.1 | New structures of TLVG. | 58 |
| A.1 | Nine experimental points in the three-dimensional space. | 65 |

Chapter 1

Introduction

1.1 Motivation

Cooking has been reported as the main source of indoor air pollution [15], which causes multiple adverse health effects such as respiration disease [7], acceleration of skin aging [15] and even lung cancer [5]. Therefore, high-performance ventilation systems are needed to remove fumes from cooking. The most common approach to improving the exhaust performance is to increase the flow rate using a centrifugal fan with a high power.

Nowadays, the flow rate of range hood can be up to $20\text{ m}^3/\text{min}$, which leads to large energy consumption and loud noise [35]. This thesis compares six types of range hoods from Chinese market. As shown in Table 1.1, the average flow rate and average noise of the range hoods in China are $15.75\text{ m}^3/\text{min}$ and 66.92 dB, respectively.

However, the flow rate of the fume generated from cooking is much lower than the flow rate of a range hood [4],[35],[16]. The great difference indicates that cooking fume is only a small part of the gas exhausted by the range hood. In view of the wide range of the range hood applied, researchers realized that it is important to improve the efficiency of the range hood for energy saving.

The efficiency of a traditional range hood is limited by its working principle [35], [2], [17]. The suction force is from the negative pressure generated by the centrifugal fan in the range hood [2], [6], and there is always a distance between the range hood and the source of the cooking fumes. The absolute value of the negative pressure decreases rapidly as the distance increases [24]. As a result, the power is insufficient to completely exhaust the cooking fumes, while clean air is a considerable part of the total gas exhausted from the range hood [23]. That is the reason for large energy waste in a traditional range hood.

Table 1.1: Parameters of different range hoods.

| Brand | Flow Rate (m^3/s) | Noise (dB) |
|--------------|---------------------------------------|--------------------------------|
| ROBAM | 17 | 67.5 |
| FOTILE | 15 | 66 |
| SIEMENS | 14.5 | 69 |
| HAIER | 17 | 68 |
| SACON | 16 | 63 |
| MIDEA | 15 | 68 |
| Average | 15.75 | 66.92 |

As for a suction system like vacuum cleaner, a pipe is used to extend the negative pressure area to the target, and the pipe directs the suction force to the target, which means that high power is not necessary even if the centrifugal fan in the vacuum cleaner is far away from the target. As for a range hood, efficiency will be significantly improved if the source of the cooking fumes is enclosed by a pipe. However, a big solid pipe is impractical in reality. Inspired by the concept of tornado in nature, a virtual gas pipe can be generated, and even heavy objects can be captured and lifted into the atmosphere because the vortex forms a rotating gas column with a strong suction force [14], [27].

Earlier research has demonstrated that two essential elements to generate tornado-like vortex are pressure difference on the vertical direction and shear force on the horizontal direction [27]. For a range hood, the centrifugal fan provides a pressure gradient only in the vertical direction. Thus, a method to provide shear force is needed to construct a micro tornado system. Meanwhile, the shear force has to match the pressure gradient to generate a stable tornado. Therefore, a novel tornado-like-vortex generator (TLVG) is proposed and built to provide the vertical pressure gradient, and the horizontal air jets from tubes are designed to provide the shear force.

1.2 Objectives

The goal of this thesis is to design and build a novel tornado-like vortex generator (TLVG) to enhance the efficiency and to reduce the noise of traditional range hood. The traditional

range hood is used to provide the vertical pressure gradient, and the horizontal air jets from the tubes of this TLVG are designed to provide the shear force.

This thesis also uses numerical simulation with ANSYS Fluent to predict both air flow path and cooking fume tracks. On the air side, incompressible air properties are adopted. Steady-state RANS approach is used with a Eulerian reference frame, and a SST $k - \omega$ equation is used to model the effects of Reynold's stresses. On the particles side, a steady-state, one-way coupled approach is used with a Eulerian reference frame, and the discrete particle model is used for the traction.

In addition, the effects of different parameters of this novel TLVG need to study. A $L_{18}(3^5)$ orthogonal experiment design is conducted to study the effects of jet velocity, flow rate of range hood, jet angle, mounting height of range hood, and distance between tubes, which are sensitive parameters to tornado-like vortex generation.

Finally, the intelligent controller is adopted to determine optimum parameters for this TLVG.

1.3 Contributions

The contributions of this thesis are as follows:

- This study makes significant contributions to the current range hood market. Existing research enhances the performance of the range hood by using greater power or air curtain. However, it does not help much with the negative pressure at the source of cooking fumes. In this thesis, a novel TLVG, which can generate two tornado-like vortices simultaneously, is designed and built, and it can increase the absolute value of the negative pressure at the source of cooking fumes significantly. Different factors of this TLVG like jet velocities and jet angles are adjustable to improve the performance and stability of the tornado-like vortices.
- This thesis explores the feasibility of using TLVG to improve range hood efficiency. Both experimental results and CFD simulation show the novel TLVG draws the smoke into the vortex column and exhaust it through the range hood rather than spreading it to the surrounding when the range hood working alone. This thesis also uses orthogonal experimental design based on the CFD results to analyze different factors of this novel TLVG, which saves time and money.

- Existing research does not enhance the performance of the range hood using Adaptive-Neural-network-based Fuzzy Inference System (ANFIS) controller. This thesis reports an intelligent controller of TLVG for different types of range hood. ANFIS is used in this intelligent controller, which utilizes the adaptability of neural network (NN) to adjust the parameters of membership functions and rules to minimize the overall error while using the Sugeno Fuzzy Inference model. The Particle Swarm Optimization (PSO) is also applied to find the globally optimal parameters of the ANFIS to optimize the ANFIS controller for a better performance.

1.4 Thesis Organization

This thesis is organized as follows:

- Chapter 2 describes the background of numerical simulation (with ANSYS FLUENT) and control theory. This chapter first introduces the computational methods within ANSYS FLUENT such as governing equations, turbulence modelling, discretization method, and discrete particle model (DPM). After that, some popular models and concepts of intelligent control theory are introduced and discussed in terms of their principles and advantages.
- Chapter 3 covers the methodology and process of this study. First, it describes the structure of experimental device: the novel tornado-like vortex generator. Second, it details the CFD modelling of the TLVG. The domain, meshes, setups, boundary conditions, and DPM settings are covered in this chapter. Then, it introduces the orthogonal experiment, and it is designed to study the effects of different factors of the novel TLVG. Last, it covers the design of the intelligent controller of the TLVG and the process of getting the training data of the controller.
- Chapter 4 compares the experiment and simulation, and it discusses the effects of different parameters such as jet velocity, range hood flow rate, radius of the vortex and the height of the range hood. In addition, it compares the standard ANFIS controller and the ANFIS with PSO controller after training.
- Chapter 5 draws the conclusion of the thesis. This chapter also discusses future works needed for this project.

Chapter 2

Background and Literature Review

2.1 Computational Method

2.1.1 Governing Equations

As for low-speed air flow case, the governing equations used in the ANSYS FLUENT solver are the incompressible Navier-Stokes equations [8], which are for the conservation equations of mass and momentum. The equation for mass conservation (equation of continuity) is:

$$\frac{\partial \rho}{\partial t} + \nabla \cdot (\rho \vec{v}) = 0 \quad (2.1)$$

Equation 2.1 is the general form of the mass conservation equation and is valid for both incompressible and compressible flows. In this thesis, the fluid is considered incompressible for low-speed air flow case (density is constant, independent of space and time), and the mass continuity equation simplifies to a volume continuity equation:

$$\nabla \cdot \vec{v} = 0 \quad (2.2)$$

The momentum conservation equation is:

$$\frac{\partial}{\partial t}(\rho \vec{v}) + \nabla \cdot (\rho \vec{v} \vec{v}) = -\nabla p + \nabla \cdot (\vec{\tau}) + \vec{F} \quad (2.3)$$

where p is the static pressure, and \vec{F} is the body force. The stress tensor $\vec{\tau}$ is given by:

$$\bar{\tau} = \mu[(\nabla \vec{v} + \vec{v}^T) - \frac{2}{3}\nabla \cdot \vec{v}I] \quad (2.4)$$

where μ is the molecular viscosity, and I is the unit tensor.

2.1.2 Turbulence Modelling

Fluctuating velocity fields describe turbulent flows. They are too computationally costly to model directly in engineering simulations since these fluctuations can be small with high frequency. Instead, to minimize the resolution of tiny sizes, the governing equations may be time-averaged, resulting in an adjusted series of equations that are less costly to solve computationally. The adjusted equations, however, contain additional unknown variables, and turbulence models are needed to calculate these variables.

This research adopts the default shear-stress transport (SST) $k - \omega$ turbulence model. The ω equation has some advantages when compared with the ϵ equation. The most influential point is that the ω equation can be integrated without additional terms in the viscous sublayer. Moreover, the $k - \omega$ model is typically more fitting for predicting the flow and separation of the boundary layer of the inverse pressure gradient. The drawback of the standard equation ω is that the solution is relatively sensitive to the values of k and ω beyond the shear layer. In ANSYS Fluent, the shear-stress transport (SST) $k - \omega$ model is recommended over the standard $k - \omega$ model.

Menter [22] proposed the shear-stress transport (SST) $k - \omega$ model to effectively combine the robust and precise formulation of the $k - \omega$ model in the near-wall region with the free-stream independence of the far-field $k - \epsilon$ model, and the equations of SST $k - \omega$ model are as follows:

$$\frac{\partial}{\partial t}(\rho k) + \frac{\partial}{\partial x_i}(\rho k u_i) = \frac{\partial}{\partial x_j} \left(\Gamma_k \frac{\partial k}{\partial x_j} \right) + \tilde{G}_k - Y_k \quad (2.5)$$

$$\frac{\partial}{\partial t}(\rho \omega) + \frac{\partial}{\partial x_i}(\rho \omega u_i) = \frac{\partial}{\partial x_j} \left(\Gamma_\omega \frac{\partial \omega}{\partial x_j} \right) + G_\omega - Y_\omega + D_\omega \quad (2.6)$$

where \tilde{G}_k and G_ω are the generation of turbulence kinetic energy due to mean velocity gradients and ω (rate of dissipation), respectively; Γ_k and Γ_ω represent the effective diffusivity of k and ω , respectively; Y_k and Y_ω are the dissipation of k and ω , respectively, due to turbulence; D_ω represents the cross-diffusion term.

2.1.3 DPM

Equations of Motion for Particles

The trajectory of a particle can be determined by integrating the force balance in the Lagrangian reference frame. The force balance equations of the particle, which is also called the trajectory equations, are:

$$m_p \frac{d\vec{u}_p}{dt} = m_p \frac{\vec{u} - \vec{u}_p}{\tau_r} + m_p \frac{\vec{g}(\rho_p - \rho)}{\rho_p} + \vec{F} \quad (2.7)$$

where m_p is the mass of the particles; \vec{u} and \vec{u}_p are the fluid phase velocity and particle velocity, respectively; ρ and ρ_p are the density of the fluid phase and the particles, respectively; \vec{F} is the additional force, including virtual force and pressure gradient force; $m_p \frac{\vec{u} - \vec{u}_p}{\tau_r}$ is drag force; τ_r is particle relaxation time:

$$\tau_r = \frac{\rho_p d_p^2}{18\mu} \frac{24}{C_d Re} \quad (2.8)$$

where μ is the molecular viscosity of the fluid phase; d_p is the diameter of the particle; Re is the relative Reynolds number, which is given by:

$$Re = \frac{\rho d_p |\vec{u}_p - \vec{u}|}{\mu} \quad (2.9)$$

Droplet Size Distributions

The Rosin-Rammler distribution is common for liquid sprays. There are several size groups, and each is represented by an average particle size, and the track of the particle is determined based on this representative particle size. The Rosin-Rammler distribution is based on the idea that an exponential relationship exists between the size of the particle (d) and the mass fraction of particles with diameter greater than d (Y_d):

$$Y_d = e^{-(d/\bar{d})^n} \quad (2.10)$$

where \bar{d} is the mean diameter and n is the spread parameter.

Turbulent Dispersion of Particles

Models of turbulent dispersion use either a stochastic discrete particle method or a cloud representation method for a group of particles with a mean trajectory. These models can also be combined to model several groups of particles with a mean trajectory involving the effects of turbulent variations in the gas phase velocities.

In this thesis, the stochastic particle tracking in turbulent flow, which is also called random track tracking, is adopted to simulate the particle turbulent movement. When the flow is turbulent, FLUENT uses the time average velocity u of the fluid to calculate the particle trajectory through the trajectory equation (Equation 2.7). The particle diffusion induced by fluid turbulence can be determined by considering the instantaneous velocity $u = u + u'$ caused by fluid velocity pulsation. The Random Walk Model is used to calculate the instantaneous velocity of the fluid.

2.2 Control Theory

2.2.1 Fuzzy System

Fuzzy logic is widely used in intelligent control with multiple inputs. Fuzzy inference is the process of input/output mapping using fuzzy logic. Fuzzy Inference Systems can model the ill-defined systems which cannot be easily modeled using mathematical equations [34]. This is because Fuzzy Inference Systems employing Fuzzy If-Then rules utilizes the qualitative nature of human reasoning in defining uncertain systems.

An example of the Fuzzy If-Then rule is like this: If the temperature is Warm then the fan speed is Fast. Quantitative identifiers like “warm” and “fast” in this example can be mathematically represented using Membership Functions. The membership function determines the probability that the crisp input satisfies our qualitative identifier, which transforms crisp inputs into fuzzy inputs.

Two inference models can be applied to inferring the output from the rule base: Mamdani’s Fuzzy inference model and Sugeno’s Fuzzy inference model.

In Figure 2.1 [12], the Mamdani’s Fuzzy inference model (type 1) evaluates the importance of each rule using the min operator and combine the outputs of all the rules using the max operator. Then, the output can be defuzzified using a defuzzification method such as center of area and mean of maximum criterion. In the Sugeno’s Fuzzy inference model (type 2), the output of each rule is expressed as a linear combination of all the inputs plus

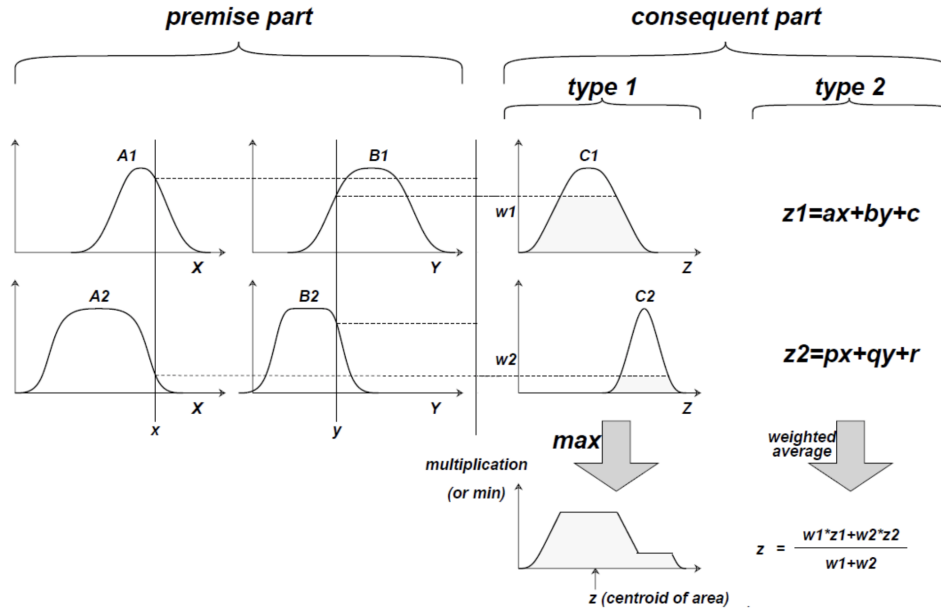


Figure 2.1: Fuzzy inference system.

a constant term [19]. Then, the final output is calculated using a weighted average of the outputs of the individual rules.

This thesis focus on the Sugeno’s fuzzy inference model. The main difference between two models is the output membership function. The Sugeno output membership functions are linear functions of x , y directly, so the result need not be defuzzified.

The Fuzzy Inference System (FIS) has some advantages. For example, the linguistic rule base models humans reasoning, which is easy to be interpreted. The parameters of FIS are also associated with the membership functions of physically meaningful quantities, which allow for selecting good initial values for them. However, the FIS also has some drawbacks. For instance, there is no standard way to generate the membership function and transform human knowledge or experience into the fuzzy rule. Therefore, an effective way is needed to tune the membership functions and the rules of the FIS.

Neural Networks represent the relationship between the inputs and outputs by a network of non-linear units. The weights of these units are modified so that their cumulative error is minimized. The neural network trains itself by learning from the available data, and it requires no prior knowledge about the system.

The goal of the Adaptive-Network based Fuzzy Inference System (ANFIS) is to combine

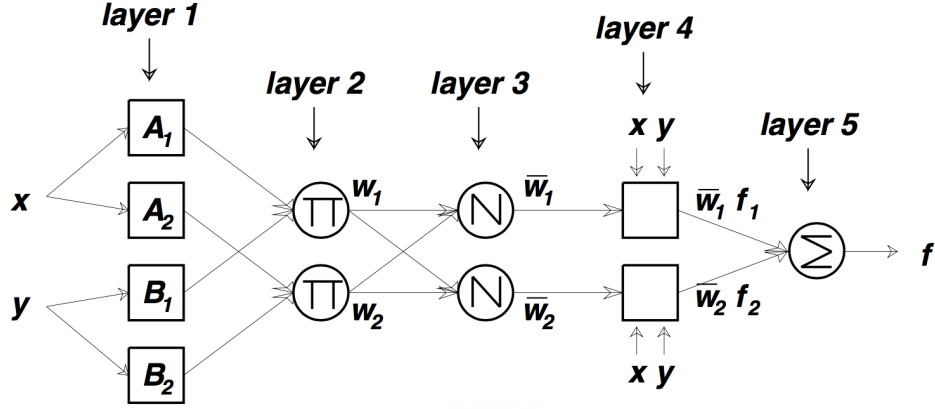


Figure 2.2: ANFIS network architecture.

the advantages of both FIS and NN. The NN is integrated into the FIS model to make it more adaptable without losing their interpretability.

2.2.2 ANFIS

ANIFS utilizes the adaptability of NN to adjust the membership functions and rules parameters to minimize the overall error while using the Sugeno Fuzzy Inference model [32]. Figure 2.2 shows a simple ANFIS with two inputs, x and y , each of which has two membership functions.

The first hidden layer of ANIFS is responsible for the membership functions and computing the membership values for system's inputs. In Figure 2.2, the membership functions of the qualitative variables A_1 , A_2 , B_1 and B_2 are μ_{A_1} , μ_{A_2} , μ_{B_1} and μ_{B_2} , respectively.

Each membership function has parameters to be learned and adapted. For example, Equation 2.11 shows the use of Gaussian function as a membership function.

$$\begin{aligned}\mu_{A_i}(x) &= \exp\left[-\left(\frac{x - a_{i1}}{b_{i1}}\right)^2\right], \\ \mu_{B_i}(y) &= \exp\left[-\left(\frac{y - a_{i2}}{b_{i2}}\right)^2\right]\end{aligned}\tag{2.11}$$

where $\{a_{i1}, a_{i2}, b_{i1}, b_{i2}\}$ are the membership functions' parameter set. These parameters control the position and width of the Gaussian functions.

| - | forward pass | backward pass |
|-----------------------|------------------------|------------------|
| premise parameters | fixed | gradient descent |
| consequent parameters | least squares estimate | fixed |
| signals | node outputs | error rates |

Figure 2.3: Two pass hybrid learning algorithm for ANFIS.

In the second layer, a T-norm operator (e.g. multiplication) is applied to the resulted membership values from the first layer. As seen in Figure 2.2, this results in w_1 and w_2 using Equation 2.12.

$$\begin{aligned} w_1 &= \mu_{A1}(x) \times \mu_{B1}(y) \\ w_2 &= \mu_{A2}(x) \times \mu_{B2}(y) \end{aligned} \quad (2.12)$$

In the third layer, the outputs of the second layer are normalized. Equation 2.13 shows the normalization used in the example of Figure 2.2.

$$\begin{aligned} \overline{w}_1 &= \frac{w_1}{w_1 + w_2} \\ \overline{w}_2 &= \frac{w_2}{w_1 + w_2} \end{aligned} \quad (2.13)$$

Note that both the second and third layers consist of mathematical operations with no learned parameters. In addition, the outputs of the third layer can be considered as the importance of each rule.

In the fourth layer, the output of each individual rule is computed using linear function of the inputs (x and y in Figure 2.2). Next, the result will be multiplied by the the respective output of the previous layer, which represent the importance of the rule. Finally, the outputs are then summed in the layer 5 to obtain the final output.

Note that, the parameters of the forth layers are learnt parameters that represent the each individual rule as illustrated in equations 2.14 to 2.15.

$$\begin{aligned} O_1^4 &= \overline{w}_1 f_1 = \overline{w}_1(p_1 x + q_1 y + r_1) \\ O_2^4 &= \overline{w}_2 f_2 = \overline{w}_2(p_2 x + q_2 y + r_2) \end{aligned} \quad (2.14)$$

$$O^5 = f = \overline{w}_1 f_1 + \overline{w}_2 f_2 \quad (2.15)$$

The parameters in layer 1 are called premise parameters, and those in layer 4 are called consequent parameters. These parameters need to be trained and updated to lower the error function, which is the error between actual and the desired output.

The original ANFIS proposed by Jang [12] uses hybrid learning, which uses gradient descent (GD) for tuning antecedent parameters and Least Square Estimate (LSE) for identifying the consequent parameters (Fig. 2.3).

In the forward pass, we can fix the parameters in the layer 1. Thus, the output is just a linear combination of the parameters in the layer4 like the Equation 2.16:

$$\begin{aligned}
 f &= \overline{w}_1 f_1 + \overline{w}_2 f_2 \\
 &= (\overline{w}_1 x) p_1 + (\overline{w}_1 y) q_1 + (\overline{w}_1) r_1 \\
 &\quad + (\overline{w}_2 x) p_2 + (\overline{w}_2 y) q_2 + (\overline{w}_2) r_2
 \end{aligned} \tag{2.16}$$

Thus, the simplest way to find the parameters is using the Least Square Estimate.

In the backward pass, we can fix the parameters in layer 4. Thus, the output is a complex nonlinear function in terms of the parameters in the layer 1. The gradient descent method is adopted to learn the parameters in layer 1 for several echoes until the error is convergent and almost 0.

2.2.3 PSO

The standard two-pass learning algorithm uses a gradient descent method that is computationally expensive and inefficient. The BP algorithm of the ANN affects the training of premise parameters, and it may fall into local minimum [13]. Various effective methods of training ANFIS networks using metaheuristic algorithms have been proposed to avoid the disadvantages of the traditional learning algorithm.

Metaheuristic algorithm is a stochastic algorithm that combines randomization and local search [31]. Their basic ideas are often from nature. Metaheuristic algorithms usually create a population of solution candidates, and they are designed for global optimization including genetic algorithms and particle swarm optimization.

Particle swarm optimization (PSO) is used widely in the process of training parameters of ANFIS. PSO is a computational method that attempts to solve problems for a given candidate solution through iterative attempts [9]. PSO solves the problem through solving a set of candidate solutions, which are the combination of the position and velocity of the particles. The motion of each particle is affected by its local optimum position and the

global optimum position for all the particles, which is updated as other particles find better positions.

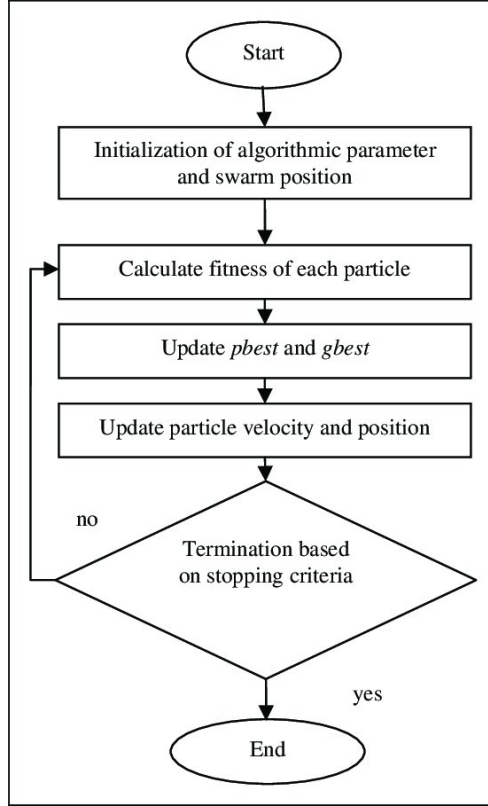


Figure 2.4: Steps in the PSO algorithm.

Figure 2.4 shows the specific steps in the PSO algorithm [1]. First, we initialize a set of random particles like the genetic algorithm (GA). For every iteration, the fitness of each particle is calculated. Then, we can get the Pbest and Gbest, which are the best position for this particle and for all the particles, respectively. After that, the particle velocity and position should be updated using this formula [25]:

$$\begin{aligned}
 V_i^{Pbest} &= Pbest - x_i^{(k)} \\
 V_i^{Gbest} &= Gbest - x_i^{(k)} \\
 V_i^{(k+1)} &= w \cdot V_i^{(k)} + c_1 \cdot V_i^{Pbest} + c_2 \cdot V_i^{Gbest} \\
 X_i^{(k+1)} &= X_i^{(k)} + V_i^{(k+1)}
 \end{aligned} \tag{2.17}$$

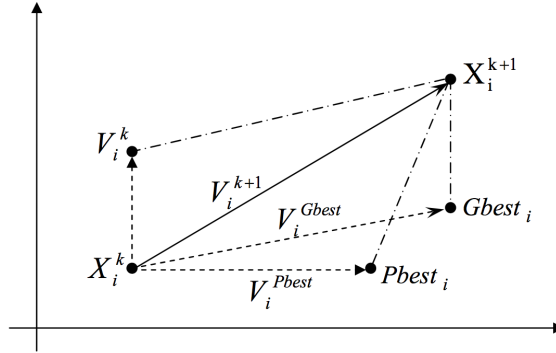


Figure 2.5: Concept of modification of a searching point by PSO.

where w is the inertia weight factor; $c1$ and $c2$ are the acceleration constants.

Figure 2.5 shows the concept of modification of the point i by PSO. The velocity of particle i at time k is expressed as $V_i^{(k)}$; V_i^{Pbest} is the velocity towards $Pbest$, and V_i^{Gbest} is the velocity towards $Gbest$. So, the velocity of particle i at time $k+1$ is a linear combination of the V_i^{Pbest} , V_i^{Gbest} and current velocity at time k $V_i^{(k)}$. Last, the updated position at time $k+1$ is the current position $X_i^{(k)}$ combine the modified velocity $V_i^{(k+1)}$. Repeating this process until the fitness converges, and then we get the best value of the parameters of the ANFIS.

Chapter 3

Methodology

3.1 Experimental Setup

Fig. 3.1 shows the aluminium frame of TLVG with the dimension of 1.1 m (length) \times 0.65 m (width) \times 2.2 m (height).

The range hood is on the top of this TLVG device. There are two popular types of range hood in the market: top-suction range hood and side-suction range hood (Fig. 3.2). In this paper, the top-suction range hood (AN-1174, Ancona, Italy) is used to test and simulate first, and the side-suction range hood (JQG9001, Fotile, China) is used to compare the results in Chapter 4. As shown in Fig. 3.3, the vertical slide guides and lock mechanisms behind the range hood are used to adjust the mounting height of the range hood above the table.

Fig. 3.4 shows three aluminium tubes with internal diameter of 48mm located on the horizontal linear slide guides under the range hood. The tube is fixed on the linear motion (LM) block on the linear slide guide using brackets. Therefore, the tubes can be moved horizontally by moving the LM block. A DC fan (FFB03812VN-SPC, Delta Electronics, Taiwan) with an air flow of 23 CFM is placed at the top end of each tube (Fig. 3.5), and the air can flow out from the holes along the side of the tube. As for the tubes on the left and right sides, each tube has 20 holes of equal diameter (5 mm) and equal distance (18 mm) from each other, and the air jets out from the holes are towards z direction. The tube in the middle has 20 in-line holes on both sides, and the air jets out from the holes are towards +x and -x directions (i.e. the lateral directions).

Fig. 3.6 shows the ultrasonic mist maker (B00P8OYGNA, AGPtek, USA) on the table of this stand. Two mist makers are used to generate visible mist to simulate cooking fumes

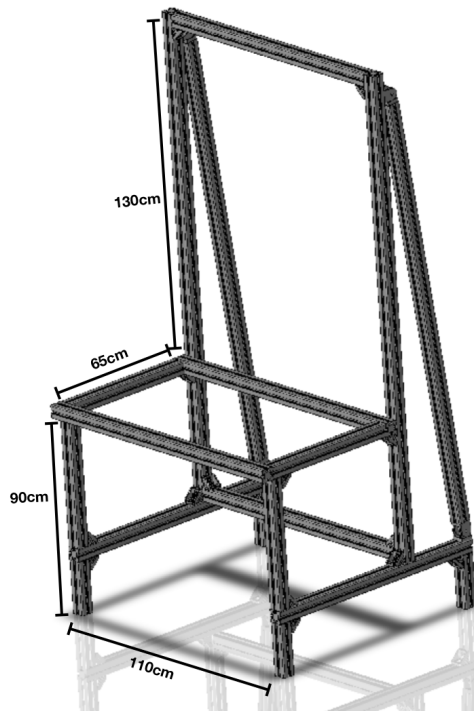
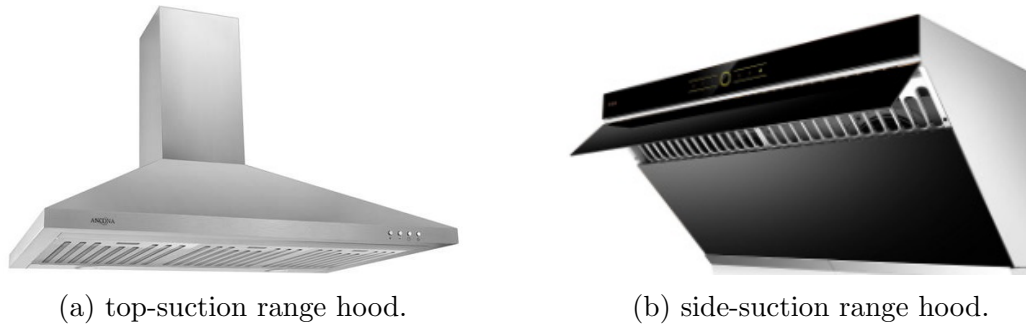


Figure 3.1: The frame of TLVG device.



(a) top-suction range hood.

(b) side-suction range hood.

Figure 3.2: Two types of range hoods.

and smoke. The black background in Fig. 3.7 is adopted to help people observe the flow path of the mist. As the concentration of mist increases, the color of the mist becomes more white. A high-speed video camera is used to capture the flow pattern of the mist.

Fig. 3.8 shows the principle of how the tornado-like vortices generated by this novel TLVG device. The top range hood provides a suction force by the negative pressure.



Figure 3.3: Vertical slide guides and lock mechanisms.

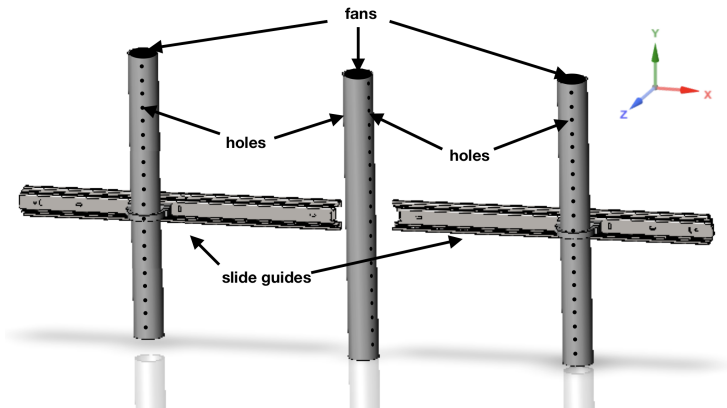


Figure 3.4: Schematic diagram of the tubes.

The jets from the holes on the tubes produce strong shearing forces, which makes the surrounding air form a tornado-like vortex and move up to the centrifugal fan of the range hood.



Figure 3.5: DC fan at end of tube.



Figure 3.6: The mist maker.

3.2 Numerical Modelling

3.2.1 Domain and Setups

Fig. 3.8 shows the 3D model of the TLVG device with the top-suction range hood built in Ansys SpaceClaim. To simulate the flow field, a cuboid with dimensions of 2.1 m (length) \times 1.15 m (width) \times 2.4 m (height) is selected as the simulation domain.

The numerical simulation is performed with Ansys Fluent 2020 R1 [3], which employs the finite volume method and the SST turbulence model by solving the three-dimensional Reynolds-averaged Navier-Stokes equations. The Discrete Phase Model is also used to



Figure 3.7: The experimental device of the TLVG.

simulate the movement of the cooking fumes. In the calculation, the indoor air is regarded as a continuous phase, and the mist is regarded as the dispersed phase that is composed of many tiny droplets.

Discretization is applied to the algebraic equations to solve the flow field. During the process of discretization, the element-based finite volume method was used to solve the steady Reynolds-averaged Navier-Stokes equations. When the flow equation was discretized in space, the pressure and momentum parts are discretized by second-order upwind scheme, and the turbulent kinetic energy part is discretized by the first-order upwind scheme. The maximum normalized residual was less than or equal to 10^{-4} for all solving variables when the algebraic equations were solved.

3.2.2 Boundary Conditions

To set boundary conditions for this model, the following assumptions were made for the physical parameters in this article:

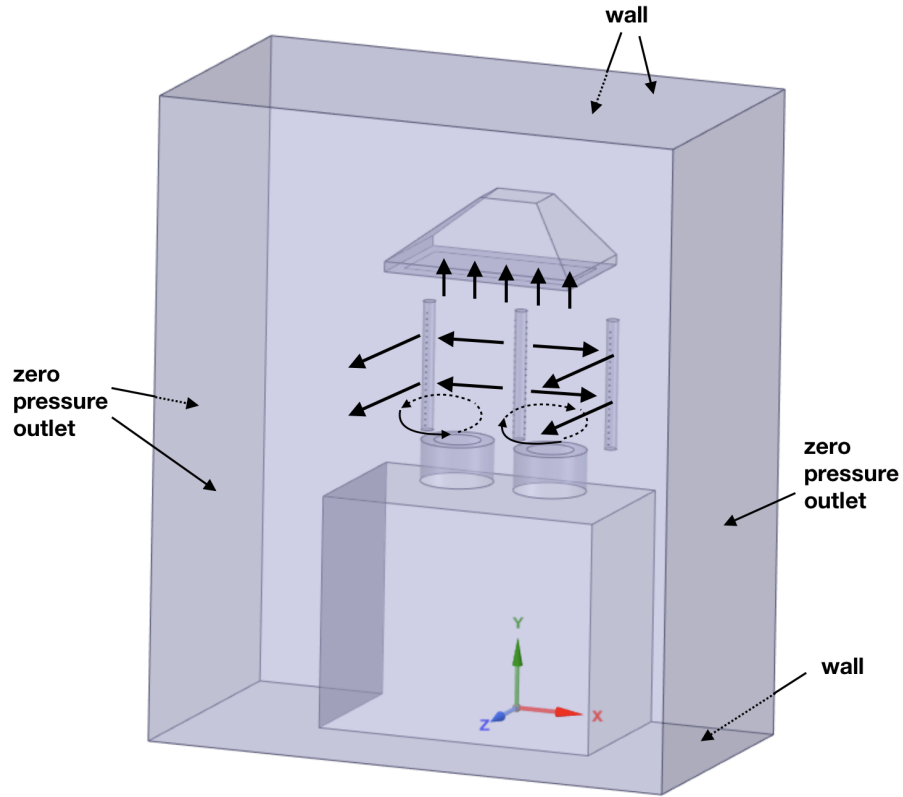


Figure 3.8: The 3D model of the TLVG.

1. The density of the fluid is considered as constant because of the low speed.
2. Considering the complex component of the cooking fumes and the various styles of cooking, only the mist phase represented the cooking fumes.
3. The steady flow is considered in the numerical simulation.
4. Other external factors such as the walking, hand movements and so on are not considered in this study.

A hand-held digital anemometer (Fig. 3.9) is used in the experiment to measure the velocity of air flow. The anemometer is fixed on the surface of the tube and covers the hole to measure the jet velocity from the hole on the surface of the tube. Different velocities



(a) Front view.

(b) Side view.

Figure 3.9: The hand-held digital anemometer.

can be measured by adjusting the voltages of the DC fan in the tube. The relationship between the voltages of the DC fan and the measured velocities is shown in Table 3.1.

Table 3.1: Jet velocities at the measuring point vs the jet velocities.

| Voltage (v) | 14 | 13 | 12 | 11 | 10 | 9 |
|-------------------------|-----|-----|------|-----|-----|-----|
| Measured velocity (m/s) | 1.3 | 1.2 | 1.15 | 1 | 0.9 | 0.8 |
| Jet velocity (m/s) | 3.1 | 2.9 | 2.7 | 2.4 | 2.2 | 2 |

However, it can cause errors due to the thickness of the anemometer. Fig. 3.9b indicates that if the anemometer is fixed on the surface of the tube, the distance between the surface of the tube and the center of the anemometer is around 2 cm. Besides, the velocity decreases rapidly because of the tiny size of the holes of the tubes. Therefore, these measured velocities can not be used as the velocity boundary conditions of the jets from the holes on the surface of the tube directly.

Assume that the velocity that we measured is the velocity 2 cm in front of the holes, and we call this point the measuring point. For analysis purposes, a horizontal line was drawn from the hole (on the surface of the tube) to the measuring point (2 cm in front of this hole). The velocities on this short line will be calculated via numerical simulation with different velocity boundary conditions at the hole (Fig. 3.10). Assume that other

factors will barely disturb the velocity results on this short line. When the velocity at the measuring point (distance = 2 cm) is the same as the measuring velocity, the velocity boundary condition at the hole (distance = 0 cm) is supposed to be the corresponding actual jet velocity. For different measured velocities, the corresponding jet velocities are listed in Table 3.1.

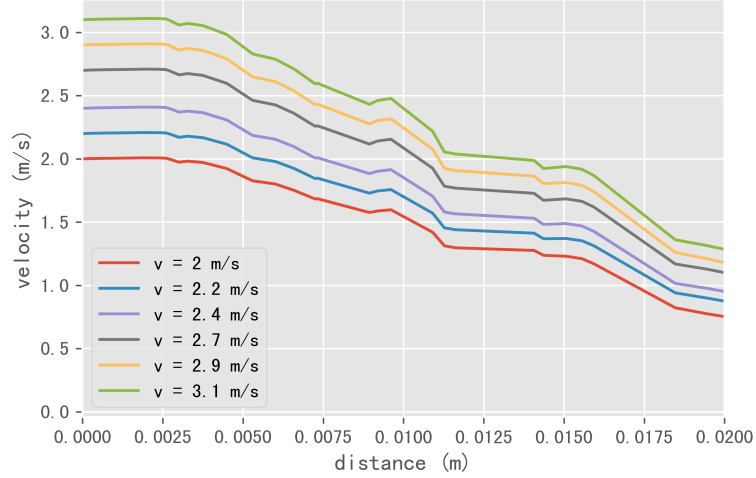


Figure 3.10: Velocities on the horizontal line from the hole to the measure point.

The top-suction range hood has a 3-speed mechanical control: 1.15 m/s, 1.43 m/s and 2 m/s, which are also measured by the digital anemometer. Because the size of the exhaust inlet surface on the bottom of the range hood is relatively big, the velocity will not decrease as fast as the that at the small holes on the tube, and the thickness of the anemometer can be neglected compared to the size of the exhaust inlet surface. Therefore, the experimental data of the exhaust flow velocities can be used directly as the boundary conditions of the exhaust inlet surface on the bottom of the range hood.

The top surface of the mist generator was the surface to release the mist. Because of the limitation of the measuring tools, the properties of the mist in this numerical simulation are from some related papers. The flow rate of the mist is set to be $1.1e-4$ kg/s [21], and the Rosin-Rammler diameter distribution with $18.6\mu m$ of mean droplet diameter and 2.76 of spread parameter is adopted [29]. As for turbulent dispersion, the discrete random walk model and random eddy lifetime with default time scale constant of 0.15 are selected.

As shown in Fig. 3.8, other external surfaces of this domain are set as zero-pressure outlet boundary conditions, and the back face, top face and bottom face of the domain

were all assumed to be no-slip wall boundary conditions, and their roughness was not considered.

3.2.3 Mesh Independence Test

Five mesh refinement levels are used to determine the dependence of the solution on the level of mesh refinement. Table 3.2 lists properties of these five levels of mesh refinements used.

Table 3.2: Five mesh levels and corresponding properties.

| Mesh level | Coarser | Coarse | Normal | Fine | Finer |
|-----------------------|---------|--------|--------|--------|---------|
| Minimum face size (m) | 0.004 | 0.002 | 0.001 | 0.0005 | 0.0001 |
| Maximum face size (m) | 0.06 | 0.06 | 0.06 | 0.06 | 0.06 |
| Nodes | 111835 | 165662 | 247814 | 368535 | 1285632 |

When the fine mesh level (nodes: 368535) is adopted, the tetrahedral mesh used to discretize the computational domain is shown in Figure 3.11. Figure 3.12 shows the mesh refinement at the hole on the surface of the tube when the minimum face size is 0.0005 m.

2 m/s of the jet velocity and 1.15 m/s of exhaust flow velocity are set as the boundary conditions in the initial modelling to find the proper mesh size. The value of static pressure and velocity of the points on the vertical central line ($x = 0.175$ m, $z = 0.15$ m) of the model is presented to compare the results. As shown in Fig. 3.13, the top end of the central line is on the range hood outlet, and the bottom end of the central line is on the table.

As shown in Fig. 3.14, the x axis is the distance below the range hood outlet, and the y axis is the value of the static pressure. The results of the pressure start to converge at the coarse mesh level, and the differences between the results at coarse mesh and the results at finer mesh are tiny to be noticed. However, it is noticed from the Fig. 3.15 that results of the velocity start to converge at the fine mesh level. For computational efficiency and result accuracy, the fine mesh (node: 368535) is selected as the final mesh in the following numerical simulations.

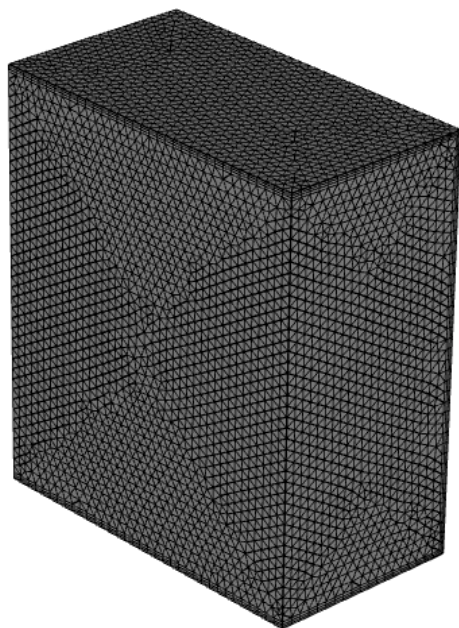


Figure 3.11: Tetrahedral mesh on the surface of the domain.

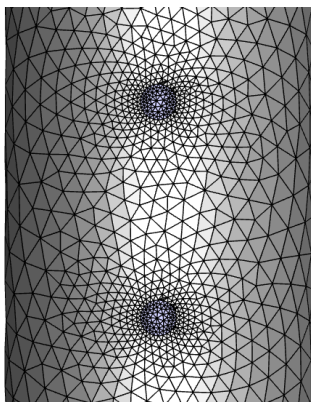


Figure 3.12: Mesh refinement at the hole on the surface of the tube.

3.3 Design of Orthogonal Experiment

To simplify the communication, some terms are introduced and defined:

- Factors: experimental variables that can be changed independently of each other.

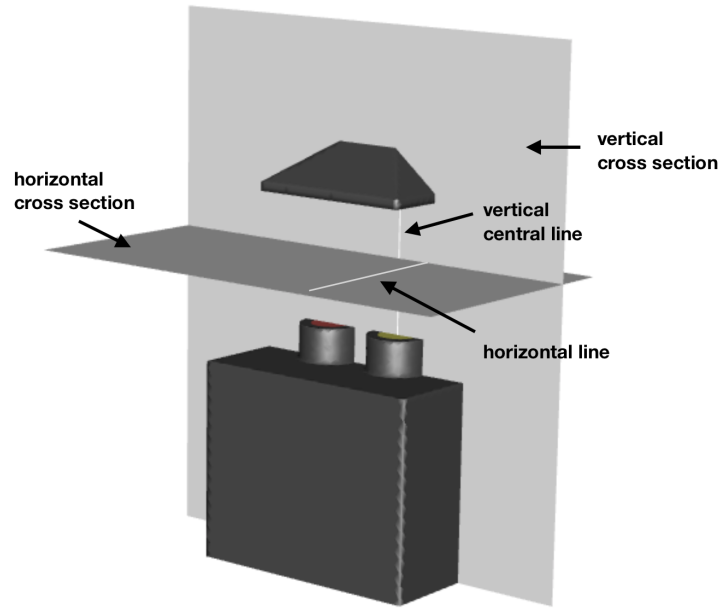


Figure 3.13: The planes of cross section, central line and horizontal line of the model.

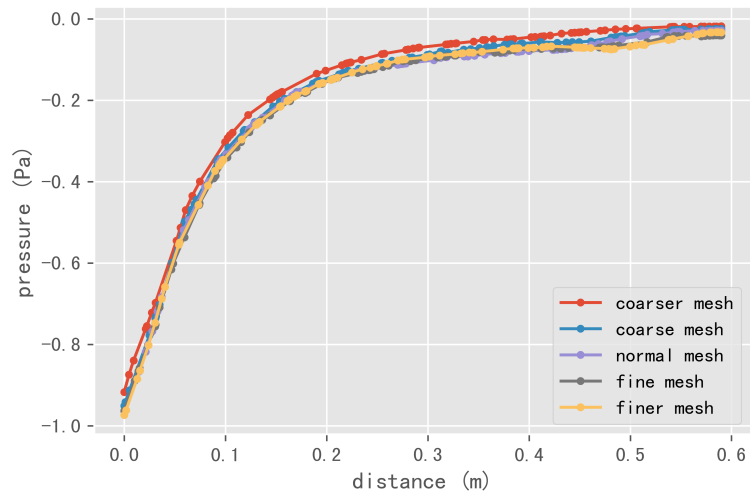


Figure 3.14: The static pressure on the vertical central line.

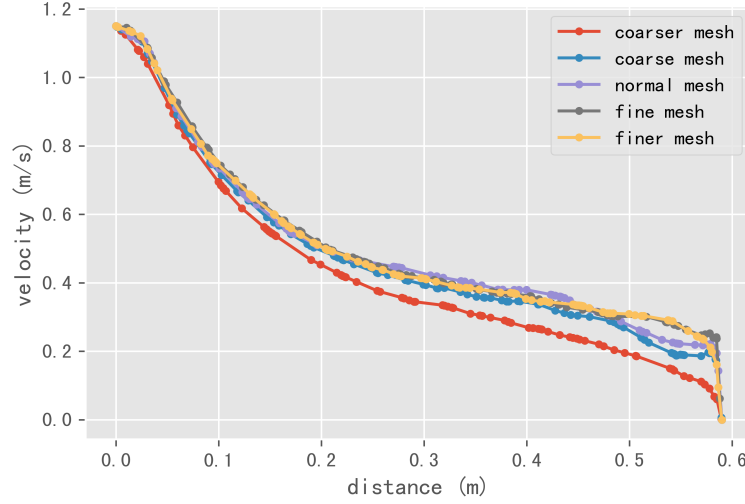


Figure 3.15: The velocity magnitude on the vertical central line.

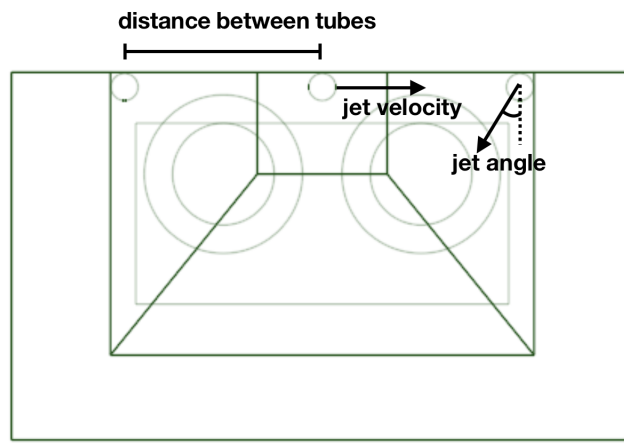
- Indices: the experimental indicators to study the effects of different factors.
- Responses: the measured value of the indices.

In this study, an orthogonal table is adopted to manage and analyze this multi-factor experiment, which can get the whole experimental results only upon part of the experiments and those analyzing conclusions [36], [20].

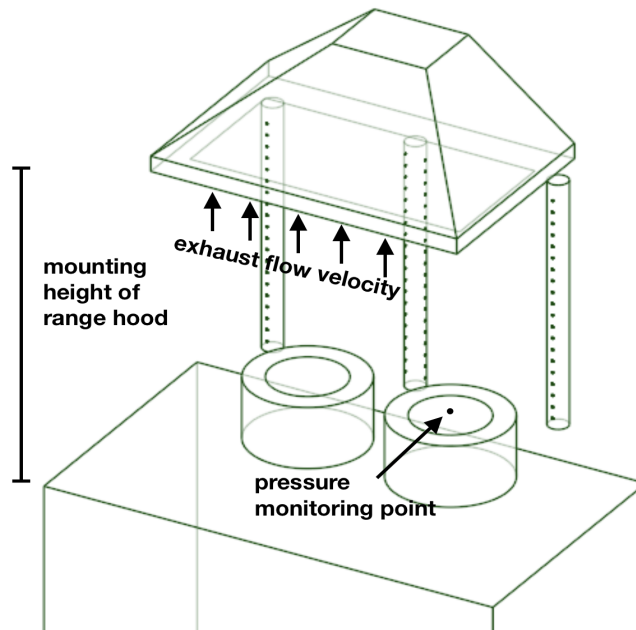
This experiment evaluates the effects of the novel TLVG on the suction of cooking fumes. Therefore, two experimental indices, the pressure at the center of the mist maker (P_{src}) and the percentage of mist particles exhausted to range hood (C_{exh}), are used to evaluate the influence of the new TLVG on the suction of cooking fumes.

In Fig. 3.16, the pressure monitoring point ($x = 0.175$ m, $y = 1.1$ m and $z = 0.15$ m), which is the at the center of the mist generator surface, is selected to measure negative pressure P_{src} . The percentage of mist exhausted to range hood (C_{exh}) can be calculated by the number of mist particles exhausted to range hood over the total number of mist particles generated by the mist generator. The greater absolute value of the negative pressure P_{src} and the higher percentage of mist exhausted to range hood C_{exh} , the better performance of this novel TLVG.

Fig. 3.16 also shows the five experimental factors considered in this orthogonal experimental design:



(a) Top View



(b) Trimetric View

Figure 3.16: Five factors in orthogonal experimental design and the pressure monitoring point.

1. The air jet velocity from the holes on the tubes.
2. The exhaust flow velocity of the range hood.
3. The jet angle of the air from the holes on the tubes.
4. The mounting height of the range hood above the table.
5. The distance between the tubes.

The relationship between the voltage of the DC fan in the tube and the jet velocity is shown on the Table 3.1. According to the experiments, the tornado-like vortex can not be generated when the voltage is lower than 9 V. Three representative levels of the jet velocity are selected to research: 2 m/s, 2.4 m/s and 2.9 m/s to process the orthogonal experimental design. As for the exhaust flow velocity of the range hood, this top-suction range hood in the experiment has 3-speed mechanical controls: 1.15 m/s, 1.43 m/s and 2 m/s, which are measured by the digital anemometer. Fig. 3.16a also shows the definition of the the angle of jet from the holes of the tube on the right side, which will be set to 0, 30 and 60 degrees in this orthogonal experimental design. In terms of the recommended mounting heights of range hood in the market, they are set to: 75 cm, 80 cm and 85 cm. Besides, the distances between tubes are set to: 30 cm, 35 cm and 40 cm. Table 3.3 presents the five orthogonal experimental factors and their three levels used in this study.

Table 3.4 is a $L_{18}(3^5)$ orthogonal table which provides 18 schemes used for the orthogonal experiments. These schemes are the different combinations of three parameter levels for five chosen factors. The rule of this $L_{18}(3^5)$ orthogonal table design is listed in the Appendix A.

Table 3.3: Factors and levels of orthogonal experimental design.

| Factors | Level 1 | Level 2 | Level 3 |
|-----------------------------------|---------|---------|---------|
| Jet velocity (m/s) | 2 | 2.4 | 2.9 |
| Exhaust flow velocity (m/s) | 1.15 | 1.43 | 2 |
| Jet angle (°) | 0 | 30 | 60 |
| Mounting height of range hood (m) | 0.75 | 0.8 | 0.85 |
| Distance between tubes (m) | 0.3 | 0.35 | 0.4 |

The multi-index comprehensive evaluation and the extreme difference analysis are adopted to deal with the experimental data more intuitively [33], [26] [11], [18], [28]. The

Table 3.4: $L18(3^5)$ orthogonal experimental plan layout.

| Scheme No. | Jet velocity (m/s) | Exhaust flow velocity (m/s) | Jet angle ($^\circ$) | Mounting height (m) | Distance (m) |
|------------|------------------------|---------------------------------|------------------------|-------------------------|------------------|
| 1 | 2 | 1.15 | 0 | 0.75 | 0.3 |
| 2 | 2 | 1.43 | 30 | 0.8 | 0.35 |
| 3 | 2 | 2 | 60 | 0.85 | 0.4 |
| 4 | 2.4 | 1.15 | 0 | 0.8 | 0.35 |
| 5 | 2.4 | 1.43 | 30 | 0.85 | 0.4 |
| 6 | 2.4 | 2 | 60 | 0.75 | 0.3 |
| 7 | 2.9 | 1.15 | 30 | 0.75 | 0.4 |
| 8 | 2.9 | 1.43 | 60 | 0.8 | 0.3 |
| 9 | 2.9 | 2 | 0 | 0.85 | 0.35 |
| 10 | 2 | 1.15 | 60 | 0.85 | 0.35 |
| 11 | 2 | 1.43 | 0 | 0.75 | 0.4 |
| 12 | 2 | 2 | 30 | 0.8 | 0.3 |
| 13 | 2.4 | 1.15 | 30 | 0.85 | 0.3 |
| 14 | 2.4 | 1.43 | 60 | 0.75 | 0.35 |
| 15 | 2.4 | 2 | 0 | 0.8 | 0.4 |
| 16 | 2.9 | 1.15 | 60 | 0.8 | 0.4 |
| 17 | 2.9 | 1.43 | 0 | 0.85 | 0.3 |
| 18 | 2.9 | 2 | 30 | 0.75 | 0.35 |

comprehensive evaluation is an effective method by which to evaluate the responses of each experimental scheme. The extreme difference analysis is employed to obtain the optimal levels for each factor and the most important factors influencing the experimental responses.

In multi-index comprehensive evaluation, the linear weighted method is very popular. In this study, the comprehensive score was calculated based on two indices: P_{src} and C_{exh} . Firstly, in order to obtain the membership degree, the maximum and minimum values of the responses of P_{src} and C_{exh} in the experimental scheme are obtained. Then the weights of P_{src} and C_{exh} were assigned to calculate the comprehensive score SC for every experimental scheme. Here, the membership degree is used to measure the influence of the experimental scheme on the P_{src} and C_{exh} respectively. Weights are used to measure the importance of P_{src} and C_{exh} by determining two fractions, and the sum of the fractions for all the indices must be 1. The calculation formula of membership degree M of index I for n-th scheme in this orthogonal experiment M_n^I is given by formula 3.1:

$$M_n^I = \frac{R_n^I - R_{min}^I}{R_{max}^I - R_{min}^I} \quad (3.1)$$

where M_n^I represents the response of index I for nth scheme in this orthogonal experiment. R_{max}^I and R_{min}^I are the maximum and minimum responses of index I respectively.

It is assumed that the pressure at the source of the mist (P_{src}) and the percentage of exhausted mist (C_{exh}) are two equally important indicators for evaluating the effectiveness of this TLVG, and the weight is 0.5 for each index. The comprehensive score SC is introduced to comprehensively assess the impact of P_{src} and C_{exh} on suction of cooking fumes. The comprehensive score for nth experimental scheme SC_n is calculated as follows:

$$SC_n = 0.5 \cdot M_n^{P_{src}} + 0.5 \cdot M_n^{C_{exh}} \quad (3.2)$$

where $M_n^{P_{src}}$ and $M_n^{C_{exh}}$ are the membership degrees of P_{src} and C_{exh} for n-th scheme, respectively.

The extreme difference analysis can obtain the most important factors affecting the experiment index and identify the optimal level combination of factors. In extreme difference analysis, the difference D is adopted to determine the main factor affecting the responses:

$$D_j = \max_i(K_{ij}) - \min_i(K_{ij}) \quad (3.3)$$

where D_j is the difference of factor j, and K_{ij} is the sum of comprehensive scores (SC) for all the schemes at ith level of factor j. $\max_i(K_{ij})$ and $\min_i(K_{ij})$ are the maximum value and the minimum value of K_{ij} for different levels of factor j. The factor with a greater D value is considered more important in affecting the responses.

3.4 Controller

3.4.1 Design of the Intelligent Controller

In real life, there are not just three levels for the exhaust flow velocity of range hood. Besides, the mounting height of the range hood may be changed according to the installation environment. Therefore, the jet velocity of TLVG should also be changed dynamically according to the changes of other factors to achieve the best performance of suction of cooking fumes. In this section, an intelligent controller is designed to control the jet velocity according to other factors measured.

In this controller, two factors are used as inputs: exhaust flow velocity and mounting height of range hood, and the jet velocity is used as output. An intelligent controller is supposed to deal with this open-loop and multiple-input system.

Fuzzy logic is widely used in intelligent control with multiple inputs. Fuzzy inference is the process of input-output mapping using fuzzy logic. Fuzzy Inference Systems (FIS) can model the ill-defined systems which cannot be easily modeled using mathematical equations. In this thesis, the Adaptive-Network-based Fuzzy Inference System (ANFIS) is used in the intelligent controller, which utilizes the adaptability of neural network to adjust the membership functions and rules parameters to minimize the overall error while using the Sugeno Fuzzy Inference model.

Figure 3.17 shows the architecture of the ANFIS for this intelligent controller. There are two inputs: the range hood flow rate (x) and mounting height of range hood (y). For each input, there are 5 Gaussian membership functions ($A_1 - A_5$ and $B_1 - B_5$) in layer 1:

$$\begin{aligned}\mu_{A_i}(x) &= \exp\left[-\left(\frac{x - a_{i1}}{b_{i1}}\right)^2\right], \\ \mu_{B_i}(y) &= \exp\left[-\left(\frac{y - a_{i2}}{b_{i2}}\right)^2\right]\end{aligned}\tag{3.4}$$

where $\{a_{i1}, a_{i2}, b_{i1}, b_{i2}\}$ are the membership functions' parameter set, which control the

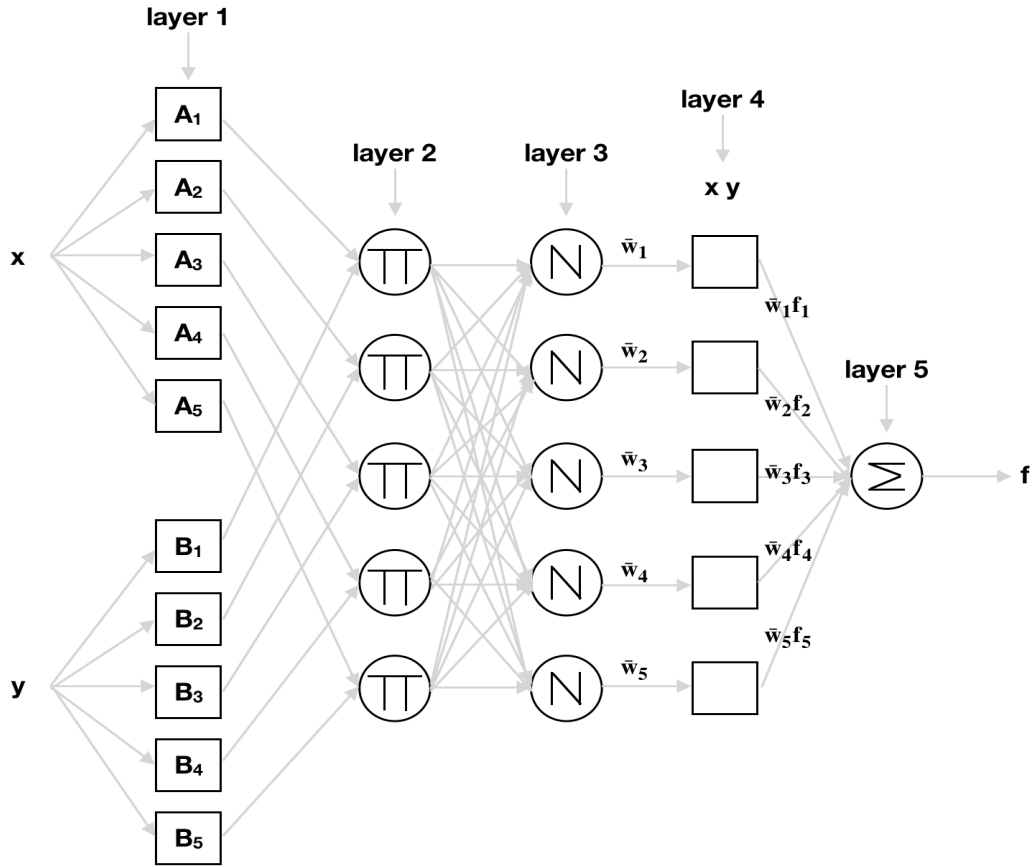


Figure 3.17: ANFIS Architecture.

position and width of the Gaussian functions. It means that this layer contains 20 ($5 \times 2 + 5 \times 2 = 20$) premise parameters for input membership functions.

In the second layer, multiplication is applied to the resulted membership values from the first layer, and the outputs of the second layer are normalized in the third layer:

$$w_i = \mu_{A_i}(x) \times \mu_{B_i}(y)$$

$$\bar{w}_i = \frac{w_i}{\sum_{i=1}^5 w_i} \quad (3.5)$$

where i is from 1 to 5, and \bar{w}_i represents the importance of each rule.

In the fourth layer, the output of each individual rule is computed using linear function

f_i of the inputs (x and y). Next, the result will be multiplied by the the respective output w_i of the previous layer:

$$\overline{w_i f_i} = \overline{w_i}(p_i x + q_i y + r_i) \quad (3.6)$$

where $\{p_i, q_i, r_i\}$ are the consequent parameters in layer 4. It means that this layer contains 15 ($5 \times 3 = 15$) consequent parameters for output membership functions.

Finally, the outputs are then summed in the layer 5 to obtain the final output:

$$f = \sum_{i=1}^5 \overline{w_i f_i} \quad (3.7)$$

The parameters in layer 1 and layer 4 need to be trained and updated to lower the error function, which is the error between system output f and the desired output.

In Matlab, a single-output Sugeno FIS can be generated and tuned based on the training data using the command: `anfis(trainingData)`. The FIS object is automatically generated using grid partitioning, and the training algorithm uses a combination of the least-squares and back propagation gradient descent methods to model the training data set.

3.4.2 Training Data

In this section, the numerical simulation results are used as the training data for the ANFIS controller. When the jet angle is 0° and the distance between tubes is 0.35 m, the tornado-like vortex with the largest radius can always be obtained, and the effect of suction of cooking fumes is the best, so the jet angle is set to 0° and the distance between tubes is set to 0.35 m. As for the exhaust flow velocity of the range hood in the market, it is usually between 1 m/s to 3 m/s. The mounting height of the range hood is from 0.75 m to 0.85 m typically.

In the numerical simulation, the exhaust flow velocities of range hood are selected as 1 m/s, 1.2 m/s, 1.4 m/s, 1.6 m/s, 1.8 m/s, 2 m/s, 2.2 m/s, 2.4 m/s, 2.6 m/s, 2.8 m/s, and 3m/s. The mounting heights of the range hood are 0.75 m, 0.8 m, and 0.85 m. Try different combinations of these two factors, and find the corresponding optimized jet velocity. The optimized jet velocity for every case is defined as the lowest velocity with the percentage of mist particles exhausted to range hood (C_{exh}) over 99%.

Repeat this process 33 (11×3) times and use this data as the training set for the ANFIS controller. While training the data, the exhaust flow velocity and the mounting height of

the range hood are the inputs, and the optimized jet velocity is the output through the neural fuzzy system. Fig. 3.18 shows that 33 training data after randomly rearrangement.



Figure 3.18: ANFIS training data.

3.4.3 ANFIS with PSO

Table 3.5: Parameters of PSO.

| parameters | number |
|---|--------|
| Population Size | 50 |
| Number of Iterations | 1000 |
| Inertia Weight w | 1 |
| Inertia Weight Damping Ratio w_{damp} | 0.99 |
| Personal Learning Coefficient c_1 | 1 |
| Global Learning Coefficient c_2 | 2 |

The parameters of the ANFIS may fall into local minimum because standard two-pass learning algorithm uses a gradient descent method. The particle swarm optimization (PSO) is applied to find the globally optimal parameters of the ANFIS to avoid the disadvantages

of the traditional learning algorithm and to design the optimal ANFIS controller with a better performance.

The algorithm of PSO is implemented in Matlab, and the script is attached in the Appendix B, which is modified according to the code given by Yarpiz [10]. Table 3.5 lists the parameters of PSO algorithms used in this script. In this script, the population size is defined as 50. The number of iterations is set as 1000, which is same as the basic ANFIS controller. The inertia weight w is 1, and the inertia weight damping ratio w_{damp} 0.99 is used to lower the inertia weight for every iteration ($w = w * w_{damp}$). Therefore, the step size will decrease after several iterations. The personal learning coefficient c_1 and the global learning coefficient c_2 are 1 and 2, respectively. After training, the output of this fuzzy logic system can be calculated using Matlab comand: *evalfis(data_name, fis_name)*. The comparison between the results of the standard ANFIS and the ANFIS with PSO after training is discussed in Chapter 4.

Chapter 4

Result and Discussion

4.1 Comparison between Experiment and Simulation

This novel TLVG device can produce two tornados on the both left and right sides at the same time. However, in the initial experiment, for simplification reasons, only one tornado on the right side is considered to research.

Scheme 1 of the orthogonal experimental design was selected to compare the CFD simulation results and the experimental results. In scheme 1, the jet velocity is 2 m/s, which means the voltage of the DC fans on the end of the tubes is 9 v according to Table 3.1. The exhaust flow velocity, jet angle, mounting height and distance between tubes are 1.15 m/s, 0° , 0.75 m and 0.3 m, respectively.

Turning on the range hood at an exhaust velocity of 1.15 m/s while turning off the air jets generator of the TLVG (i.e. the conditions of not generating a tornado-like vortex) as shown in Fig. 4.1a, it can be observed that the mist is spreading out at the bottom region due to its higher density than that of air. The suction force from the centrifugal fan in the range hood is not strong enough to lift up the mist particles. Turning on both the range hood at an exhaust velocity of 1.15 m/s and the air jets generator at a velocity of 2 m/s in the middle and right tubes, the mist rapidly forms a tornado-like vortex on the right side of this device. It is like a virtual pipe connecting the source of the mist and the centrifugal fan of the range hood. Almost all the mist is going to the range hood, and no more spreading can be observed as shown in Fig. 4.1b.

As for the numerical simulation, Fig. 4.2 shows an intuitive view of the mist particles tracking, which is similar to what is observed in the experiment (Fig. 4.1). Fig. 4.2a shows



(a) Turning on the range hood while turning off the air jets generator.



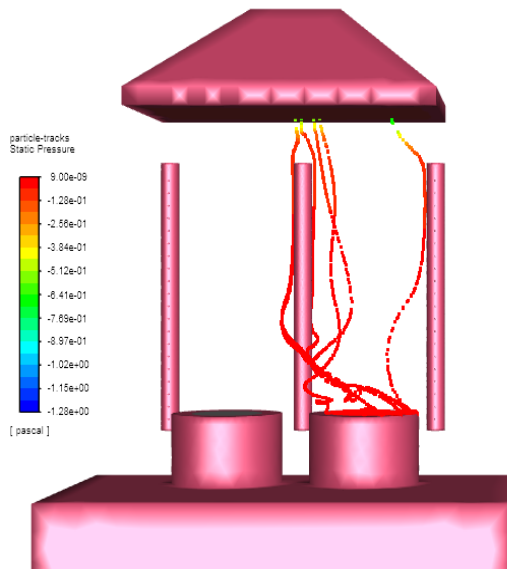
(b) Turning on both the range hood and the air jets generators (middle and right tubes).

Figure 4.1: Mist distribution comparison.

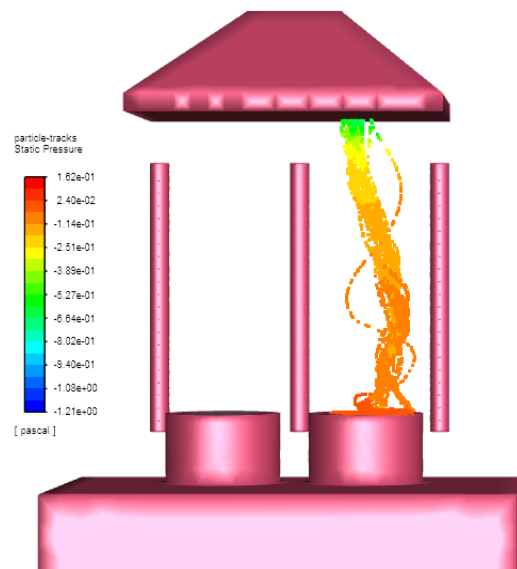
the case turning on the range hood at a speed of 1.15 m/s while turning off the air jets generator, and most of the mist is stay at the bottom and only little portion of mist is sucked up by the range hood. Fig. 4.2b shows the case turning on both the range hood at speed of 1.15 m/s and the air jets generator at a speed of 2 m/s on the middle and right tubes, and the mist is exhausted through the tornado-like vortex which has been seen in Fig. 4.1b.

Similarly, Fig. 4.3 shows an intuitive view of the negative pressure region (non-red region) comparing the cases without and with the TLVG device on the vertical cross section ($z = 0.15$ m) in Fig. 3.13. The mist maker is far away from the range hood, but the negative pressure region is expanded in the vertical direction to draw the water mist around the mist maker in Fig. 4.3b.

As shown in the Fig. 3.13, a horizontal line ($x = 0.35$ m, $y = 1.308$ m) was drawn

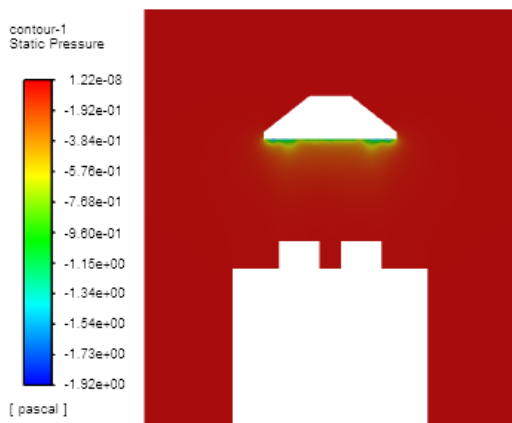


(a) Turning on the range hood while turning off the air jets generator.

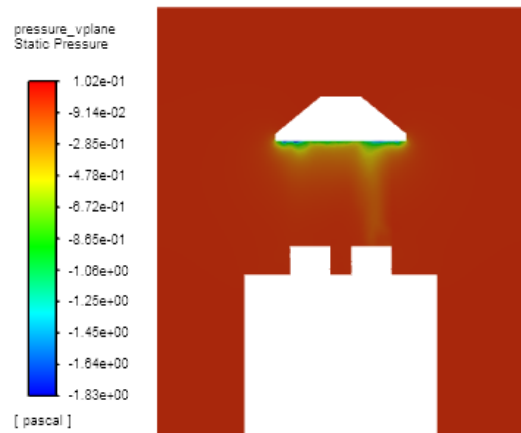


(b) Turning on both the range hood and the air jets generator (middle and right tubes).

Figure 4.2: Particle tracking comparison.



(a) Turning on the range hood while turning off the air jets generator.



(b) Turning on both the range hood and the air jets generator (middle and right tubes).

Figure 4.3: Static pressure comparison.

directly in front of the holes of the tube on the right side. The values of the velocity on this line compare the simulation with the experimental result. As shown in the Fig. 4.4, the red line represents the velocities of the points on this horizontal line which are calculated through numerical simulation. Meanwhile, the discrete points are the results measured by the digital anemometer. Notice that there are errors for the values measured by the digital anemometer, but the trends of results between simulation and experiment in Fig. 4.4 are consistent, and the errors between them are deemed acceptable.

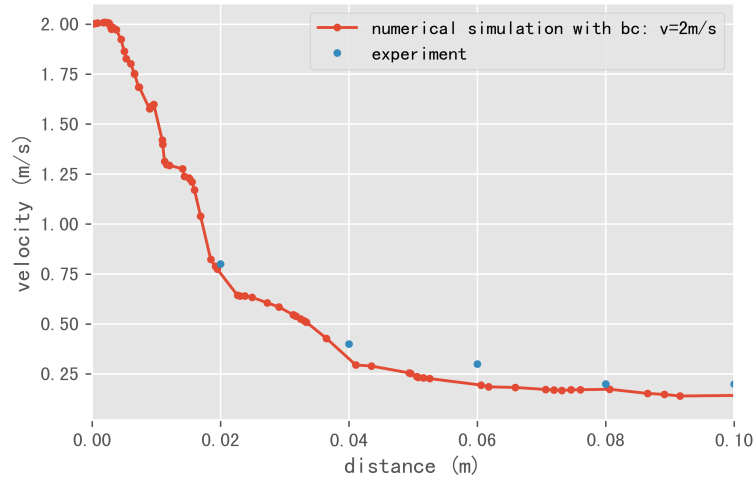


Figure 4.4: The static pressure on the central line.

All these similarities and matched data of the experimental and numerical results indicate that the numerical model has successfully captured the main features, and the results of the CFD simulation are reliable.

4.2 Results of Orthogonal Experimental Design

Table 4.1 presents the results of the orthogonal experimental design, in which the responses for $-P_{src}$ (-Pa) and C_{exh} of each schemes and the corresponding membership degree M and the comprehensive score SC obtained through Equations 3.1 and 3.2 are listed.

As shown in Table 4.1, when experimental scheme 17 was adopted, the P_{src} , C_{exh} , $M_{P_{src}}$ and $M_{C_{exh}}$ are -0.1912 Pa, 97.65%, 1 and 1, respectively. This indicates that the negative pressure at the center of the mist maker (P_{src}) can be enhanced obviously and the

Table 4.1: Results of orthogonal experiment.

| Scheme No. | $-P_{src}$ (-Pa) | C_{exh} (%) | $M_{P_{src}}$ | $M_{C_{exh}}$ | SC |
|------------|------------------|---------------|---------------|---------------|-------|
| 1 | 0.0805 | 70.37 | 0.340 | 0.609 | 0.474 |
| 2 | 0.0632 | 68.52 | 0.237 | 0.582 | 0.410 |
| 3 | 0.0468 | 52.44 | 0.139 | 0.351 | 0.245 |
| 4 | 0.1034 | 58.64 | 0.477 | 0.440 | 0.459 |
| 5 | 0.0440 | 65.85 | 0.123 | 0.544 | 0.333 |
| 6 | 0.0456 | 45.68 | 0.132 | 0.254 | 0.193 |
| 7 | 0.0368 | 59.01 | 0.080 | 0.446 | 0.263 |
| 8 | 0.0491 | 27.95 | 0.153 | 0.000 | 0.077 |
| 9 | 0.1776 | 80.86 | 0.919 | 0.759 | 0.839 |
| 10 | 0.0316 | 63.58 | 0.049 | 0.511 | 0.280 |
| 11 | 0.0692 | 52.17 | 0.273 | 0.347 | 0.310 |
| 12 | 0.0592 | 42.24 | 0.213 | 0.205 | 0.209 |
| 13 | 0.0920 | 84.12 | 0.409 | 0.806 | 0.607 |
| 14 | 0.0393 | 59.63 | 0.095 | 0.455 | 0.275 |
| 15 | 0.1227 | 63.58 | 0.592 | 0.511 | 0.551 |
| 16 | 0.0234 | 57.41 | 0.000 | 0.423 | 0.211 |
| 17 | 0.1912 | 97.65 | 1.000 | 1.000 | 1.000 |
| 18 | 0.1422 | 80.75 | 0.708 | 0.758 | 0.733 |

maximum percentage of mist exhausted to ranged hood C_{exh} was obtained when the jet velocity, the exhaust flow velocity of the range hood, the jet angle, the mounting height of the range hood and distance between tubes were 2.9 m/s, 1.15 m/s, 0, 0.85 m and 0.3 m, respectively when experimental scheme 17 was adopted.

For factor j, the K values for level a, b and c as well as the D values were calculated using Equation 3.2 and Equation 3.3. Their values are listed in Table 4.2. The level with the higher value of K is considered to provide better control effectiveness for the cooking fumes. For example, for the factor of jet velocity, level c (2.9 m/s) performs the best

Table 4.2: Extreme difference analysis of orthogonal experiment.

| Factor | Jet velocity | Exhaust flow velocity | Jet angle | Mounting height | Distance between tubes |
|----------|--------------|-----------------------|-----------|-----------------|------------------------|
| K_{aj} | 1.929 | 2.294 | 3.634 | 2.248 | 2.561 |
| K_{bj} | 2.419 | 2.404 | 2.555 | 1.917 | 2.995 |
| K_{cj} | 3.122 | 2.771 | 1.281 | 3.305 | 1.914 |
| D_j | 1.194 | 0.477 | 2.352 | 1.388 | 1.080 |

because 3.122 is the highest among all the K values for three levels. Similarly, level c (2 m/s) of the factor of exhaust flow velocity, level a (0°) of the factor of jet angle, level c (0.85 m) of the factor of mounting height and level b (0.35 m) of the factor of distance between tubes performs the best. In Table 4.2, the D value of factor jet angle was higher than those of other factors. This means that the effect of the jet angle of this TLVG on the pressure and concentration of escaped cooking fumes is significant, and the horizontal jet angle should always be 0 to get the best performance. The D value of factor exhaust flow velocity is the lowest among D values of all the factors, which indicates that the exhaust flow velocity only slightly impacts the effects of the TLVG on the suction of cooking fumes.

4.3 Effects of Different Factors on Tornado-Like Vertex

4.3.1 Jet Velocity

Different jet velocities are tested in this section while other irrelevant variables are fixed. From the results of the orthogonal experiment, the proposed responses for the factors of exhaust flow velocity of the range hood, the jet angle, the mounting height and the distance between tubes are 2 m/s, 0° , 0.85 m, and 0.35 m, respectively.

To assess the effect of the jet velocity on tornado-like vertex, the values of static pressure of the points on the vertical central line of the model in Fig. 3.13 are presented to compare the results. In Fig. 4.5, the x-axis is the distance below the range hood, and the y-axis is the corresponding static pressure. The pressure tends to be 0 when the distance is far away from the range hood. Different lines in Fig. 4.5 represent cases with different boundary conditions of the jet velocities at the holes of the tubes. Higher jet velocity generally

produces higher absolute value of negative pressure due to the larger shearing force, which will be helpful to concentrate and suck up the cooking fumes. Fig. 4.6 shows the velocity vector on the horizontal cross section ($y = 1.308 \text{ m}$) in Fig. 3.13 at different jet velocities, which indicates that the radius of the tornado-like vortex becomes larger as the jet velocity increases.

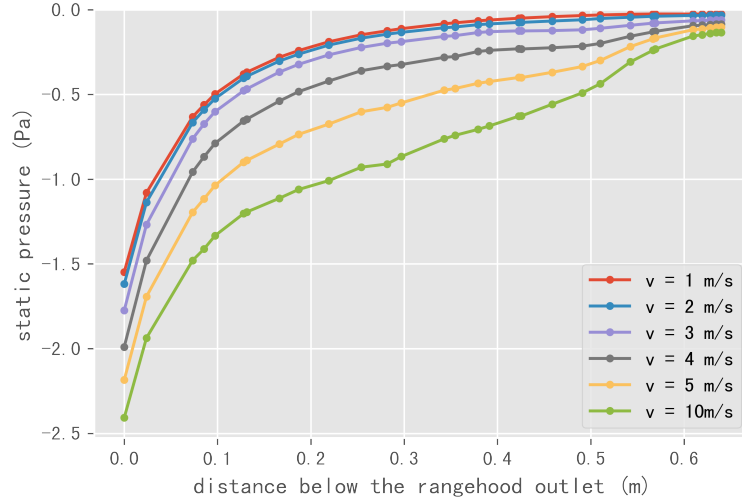


Figure 4.5: Pressure on the central line with different jet velocities.

However, the particle size of mist is relatively small (around $0.01 - 10 \mu\text{m}$ [30]), which means that strong suction force is not necessary for this TLVG. Because higher jet velocity consumes more power, a trade off must be made between exhausting efficiency and power losses. The results of the percentage of particles exhausted to the range hood are summarized in Table 4.3. Although the absolute value of negative pressure and the radius of the tornado-like vortex will be greater when the jet velocity increases, the percentage of particles exhausted to the range hood has reached 100% when the boundary condition of the jet velocity at the holes of the tube is 4 m/s.

Table 4.3: Percentage of exhausted particles for different jet velocities.

| Jet velocity (m/s) | 1 | 2 | 3 | 4 | 5 | 10 |
|--------------------|-------|-------|-------|-----|-----|-----|
| Percentage (%) | 47.92 | 64.58 | 83.33 | 100 | 100 | 100 |

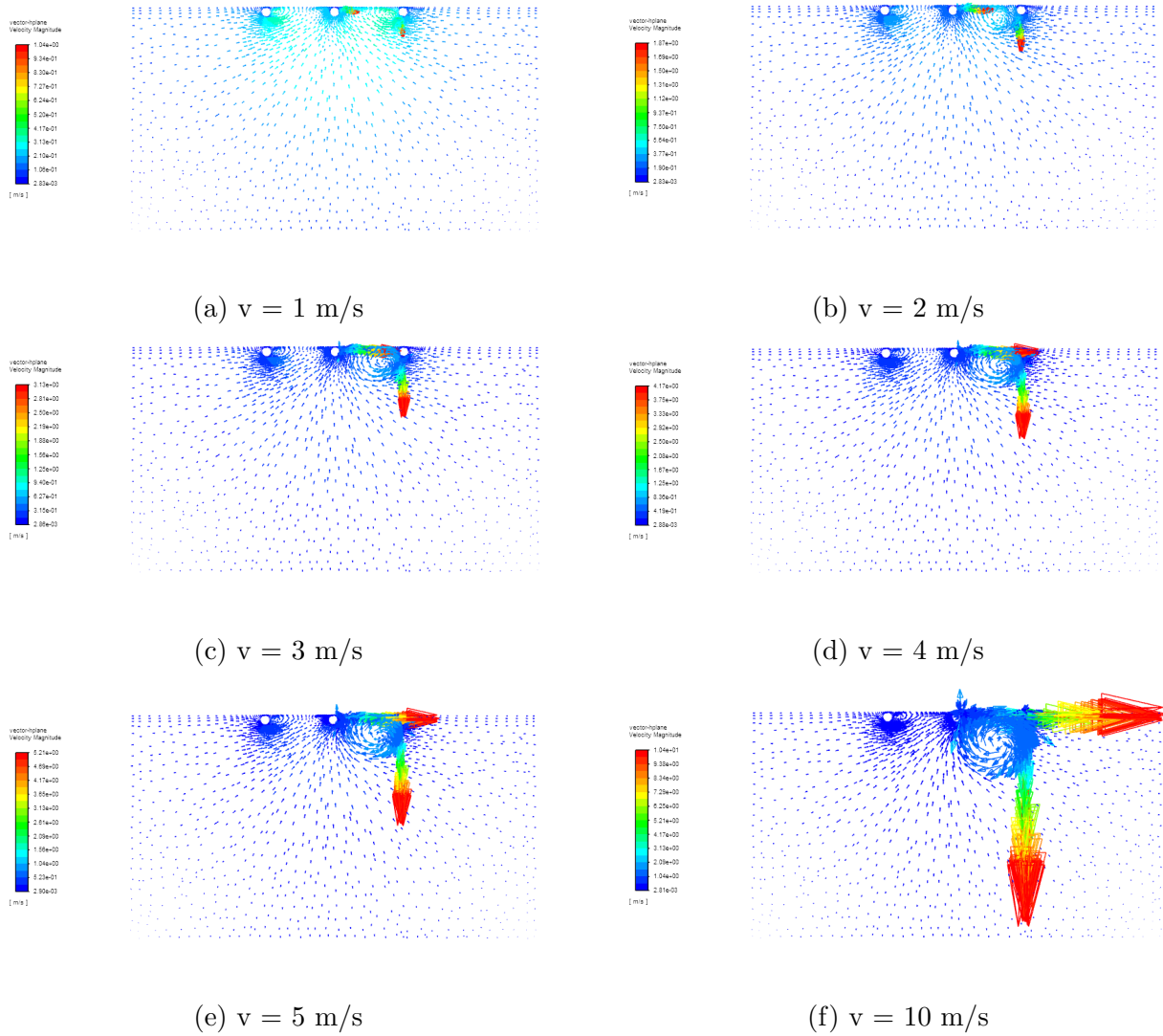


Figure 4.6: Velocity vector on the horizontal cross plane with different jet velocities.

4.3.2 Range Hood Exhaust Flow Velocity

In reality, there are more than these three speeds for a range hood. Therefore, different exhaust flow velocities have been tested in this section while other irrelevant variables are fixed. From the results of the orthogonal experiment above, the proposed factors for the jet velocity, the jet angle, the mounting height and the distance between tubes are 2.9 m/s,

0°, 0.85 m and 0.35 m respectively.

The values of static pressure of the points on the vertical central line (Fig. 3.13) of the model are also presented to compare the results. As shown in Fig. 4.7, higher exhaust flow velocity results in greater absolute value of negative pressure at the exhaust hood. However, the pressure does not change much at the mist source area far away from the range hood.

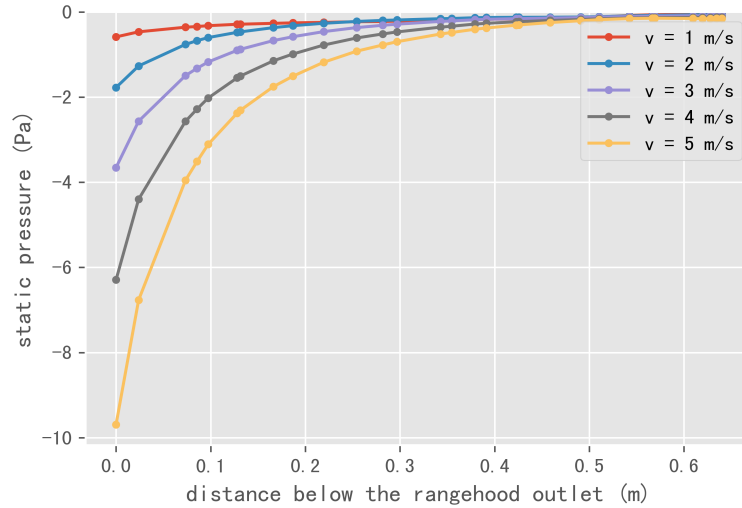
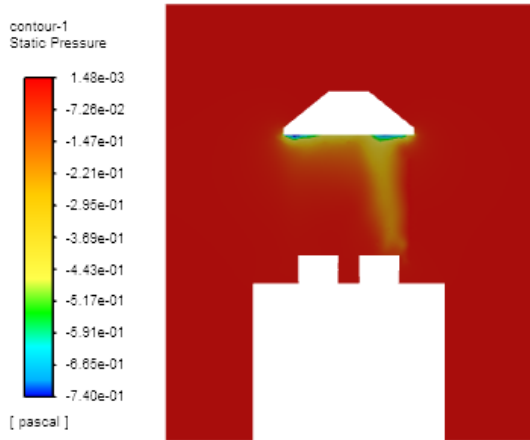


Figure 4.7: Pressure on the central line with different exhaust flow velocities.

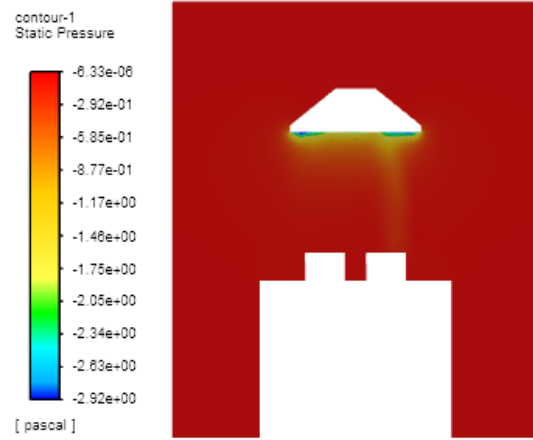
From Table 4.4, the percentage of particles exhausted to the range hood decreases as the exhaust flow velocity increases. Besides, as seen in Fig. 4.8, the tornado-like vortex fades away when the exhaust flow velocity increases. These figures indicate that higher power of range hood cannot guarantee the performance of the tornado-like vortex generator.

Table 4.4: Percentage of exhausted particles for different exhaust flow velocities.

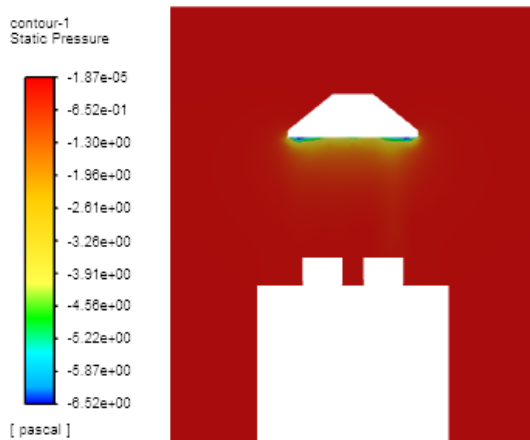
| Exhaust flow velocity (m/s) | 1 | 2 | 3 | 4 | 5 |
|-----------------------------|-----|-------|-------|-------|----|
| Percentage (%) | 100 | 83.33 | 64.58 | 64.58 | 50 |



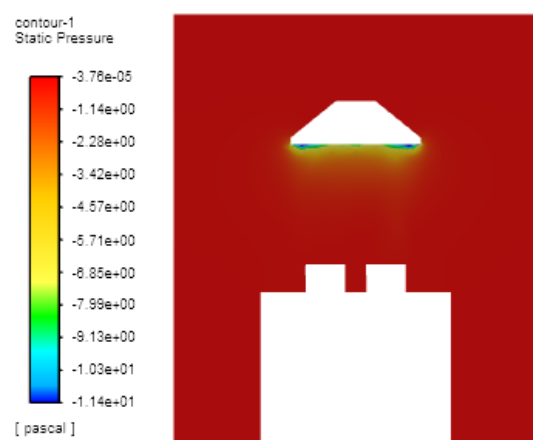
(a) Exhaust flow velocity = 1 m/s



(b) Exhaust flow velocity = 2 m/s



(c) Exhaust flow velocity = 3 m/s



(d) Exhaust flow velocity = 4 m/s

Figure 4.8: Pressure contour on the vertical cross plane with different jet velocities.

4.4 Interaction between Two Tornado-like vortices

In this section, the results of the orthogonal experiment for the right part of TLVG are applied to both left and right parts of TLVG. The proposed responses for the factors of jet velocity, exhaust flow velocity, the jet angle, the mounting height and the distance between

tubes are 2.9 m/s, 2 m/s, 0, 0.85 m, and 0.35 m, respectively.

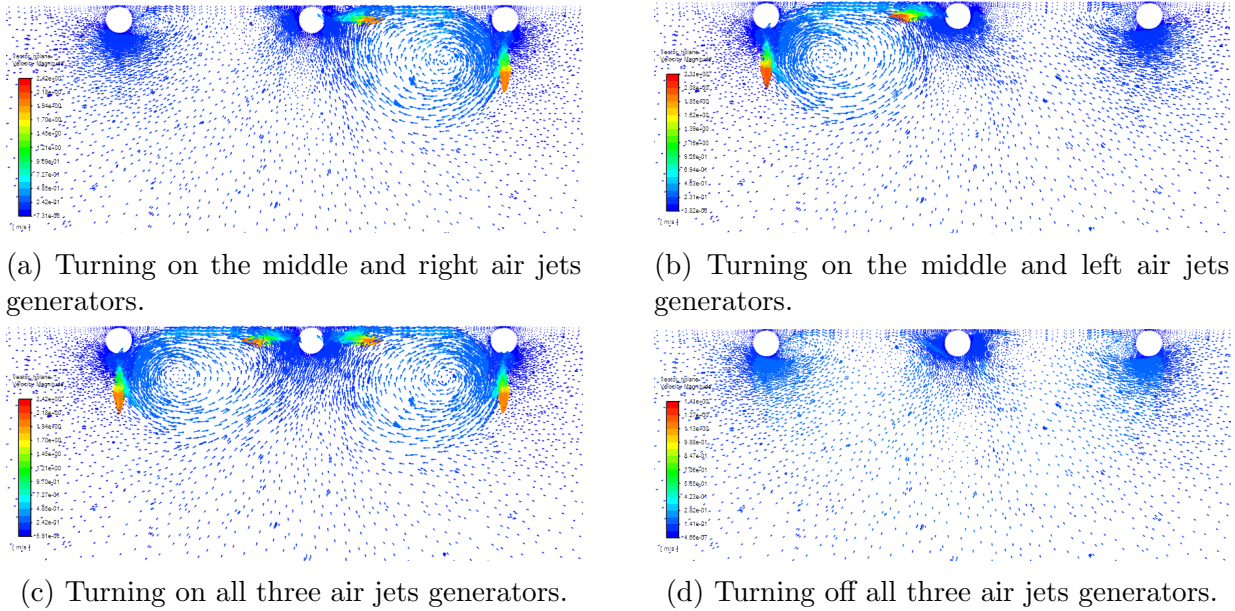


Figure 4.9: Velocity vector on the horizontal cross plane.

Keeping the range hood on (exhaust flow velocity of 2 m/s), there are four cases considered in this section: (a) Turning on the DC fans in the right tube and middle tube, the tornado-like vortex can be produced on the right part of the TLVG; (b) turning on the DC fans in the left tube and middle tube, the tornado-like vortex can be produced on the left part of the TLVG; (c) turning on all the DC fans in these three tubes, two tornado-like vortices can be produced at the same time; (d) turning off all the DC fans in these three tubes, no tornado-like vortex is produced.

The velocity vectors on the horizontal plane are shown in the Fig. 4.9. Two vortices in the third case are separated, and the shapes of two vortices are not affected by each other.

For case (a), only the mist maker on the right side is turned on. For case (b), only the mist maker on the left side is turned on. For case (c) and (d), both two mist makers are turned on. The results of the mist particles tracking are summarized in Table 4.5. In this table, different number of tries are used in the discrete random walk model. If the number of tries is greater than or equal to 1, then Ansys Fluent will consider the influence of turbulence on particles in the particle force balance equation when calculating the particle trajectory. If the number of tries is greater than 1, the particle trajectory will be

Table 4.5: Percentage of exhausted particles for 4 cases

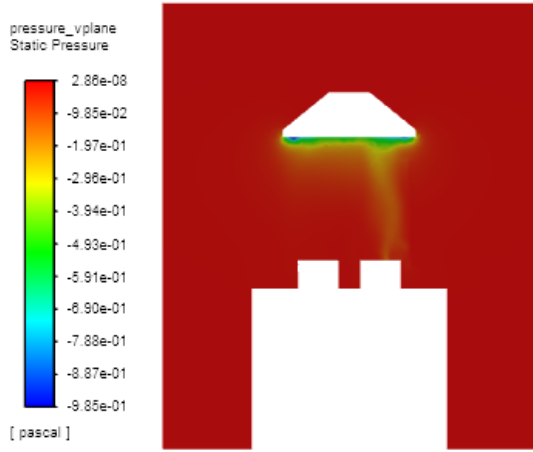
| Number of tries | Case a | Case b | Case a + Case b | Case c | Case d |
|--------------------|-------------|-------------|-----------------|-------------|------------|
| 1 | 489 / 636 | 569 / 624 | 1058 / 1260 | 1035 / 1260 | 103 / 1260 |
| 2 | 988 / 1272 | 1138 / 1248 | 2126 / 2520 | 2075 / 2520 | 208 / 2520 |
| 3 | 1473 / 1908 | 1706 / 1872 | 3179 / 3780 | 3102 / 3780 | 309 / 3780 |
| 4 | 1961 / 2544 | 2274 / 2496 | 4235 / 5040 | 4134 / 5040 | 410 / 5040 |
| 5 | 2453 / 3180 | 2844 / 3120 | 5297 / 6300 | 5182 / 6300 | 523 / 6300 |
| Average | 0.77 | 0.91 | 0.84 | 0.82 | 0.08 |
| Standard deviation | 0.0029 | 0.0003 | 0.0015 | 0.0013 | 0.0007 |

calculated multiple times. For each trajectory calculation, a new random representation of the turbulent is used in the particle balance equation. If the particle trajectory is calculated several times, then the trajectory calculation includes the statistical characteristic quantities of the particle flow affected by turbulence.

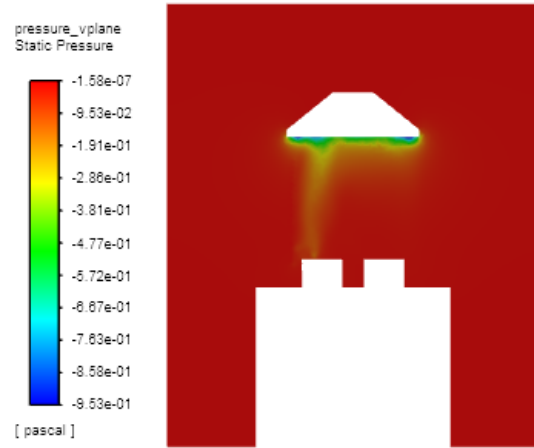
As we see from the Table 4.5, the percentage of exhausted particles in the case a and case b (average: 84%) is always a little bit greater than that of the case c (average: 82%), which means that the effects of the novel TLVG on the suction of cooking fumes will decrease a little bit when three jets generators turning on at the same time in case c. Nevertheless, the effects on the suction of cooking fumes of case c is much better than that of case d (average: 8%). Fig. 4.10 shows the corresponding pressure contours on the vertical plane. It can be noticed that in the case c, the absolute value of the negative pressure around the mist maker is less than those of case a and case b, but it is still much greater than that of case d. Fig. 4.11 shows the experimental results for these four situations, which are consistent with the simulation results.

4.5 Side-Suction Range Hood

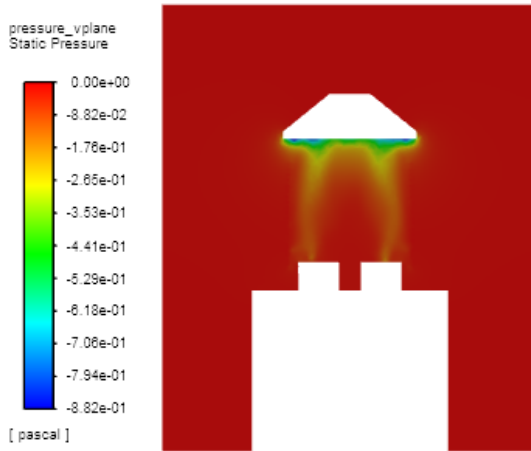
A side-suction range hood is also tested on this TLVG device to adapt to all the popular types of range hood on the market. The main difference between the top-suction range hood and side-suction range hood is the position of the exhaust outlet. As shown in Fig. 4.12, the exhaust outlet is on the side of the range hood, and it is close to the front of the table. From Fig. 4.12, because the volume of the side-suction range hood is greater than



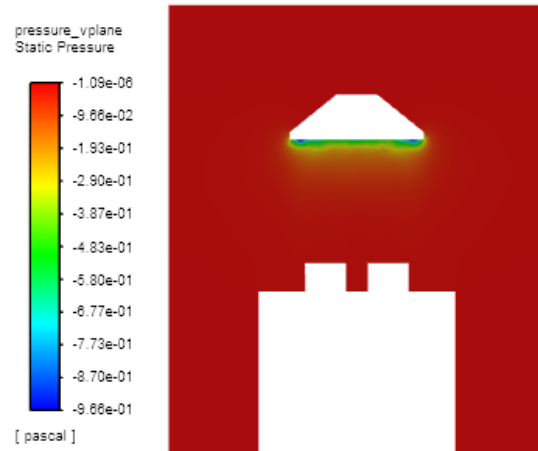
(a) Turning on the middle and right air jets generators.



(b) Turning on the middle and left air jets generators.



(c) Turning on all three air jets generators.



(d) Turning off all three air jets generators.

Figure 4.10: Pressure contour on the vertical cross plane.

that of the top-suction range hood, the length of the tube need to be shorter, which results in fewer flow rate of air jets.

The results of the orthogonal experiment are also applied to the TLVG with side-suction



(a) Turning on middle and right jets generators. (b) Turning on middle and left jets generators.



(c) Turning on all three air jets generators. (d) Turning off all three air jets generators.

Figure 4.11: Mist distribution comparison in the experiment.

range hood. The proposed responses for the factors of jet velocity, exhaust flow velocity, the jet angle, the mounting height and the distance between tubes are 2.9 m/s, 2 m/s, 0, 0.85 m, and 0.35 m, respectively. The pressure contours on the vertical plane are shown in Fig. 4.13, and the path lines of the jet flow from the holes of the tubes are shown in

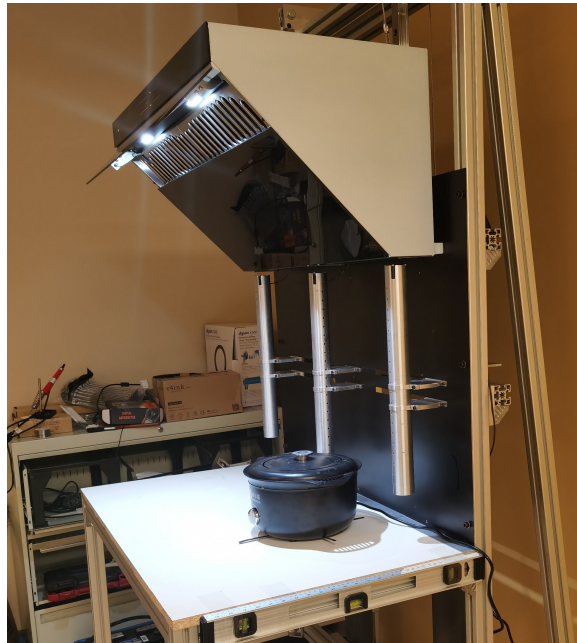


Figure 4.12: The side-suction range hood.

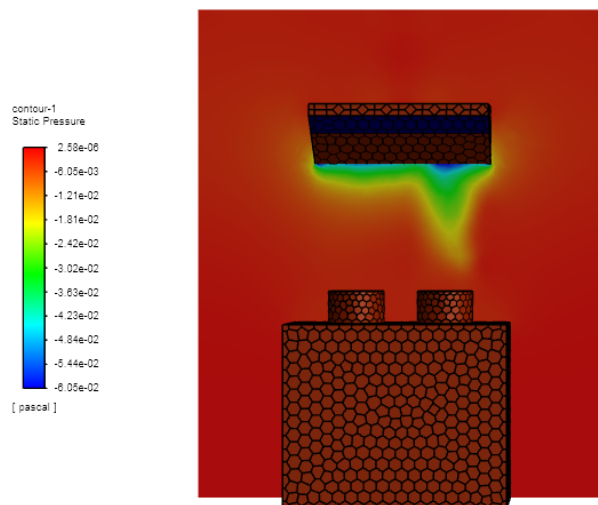


Figure 4.13: Pressure on the vertical plane with side-suction range hood.

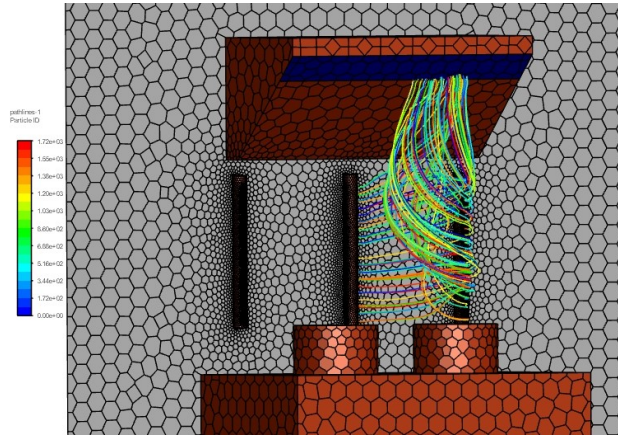


Figure 4.14: Pathline of jet flow with side-suction range hood.

Fig. 4.14. From Fig. 4.13, it shows that the absolute value of the negative pressure for side-suction range hood is generally less than that for top-suction range hood, which is caused by the further distance between the exhaust outlet and the mist maker and the less flow rate of air jets. However, these two figures indicate that the tornado-like vortex can also be generated for a side-suction range hood, and effect on suction of cooking fumes is better than that of side-suction range hood without TLVG.

4.6 Intelligent Controller of TLVG

4.6.1 Results of Standard ANFIS

Fig. 4.15 shows the architecture of ANFIS controller generated by Matlab Simulink. After training the 33-rows training data for maximum 1000 iterations, Figure 4.16a shows the 5 optimized membership functions for exhaust flow velocity of range hood, and Figure 4.16b shows the 5 optimized membership functions for mounting height.

Figure 4.17 shows surface plot showing relationship between two inputs and one output after trained. Input 33-row checking data using this fuzzy logic system after training, the results are in Figure 4.18. The sub-figure on the top compares the checking data and the ANFIS system outputs. The blue line represents the checking data outputs, and the red line represents the standard neural fuzzy system real outputs. The sub-figures on the bottom shows the errors for each sample. They indicate that the mean squared error (MSE) and

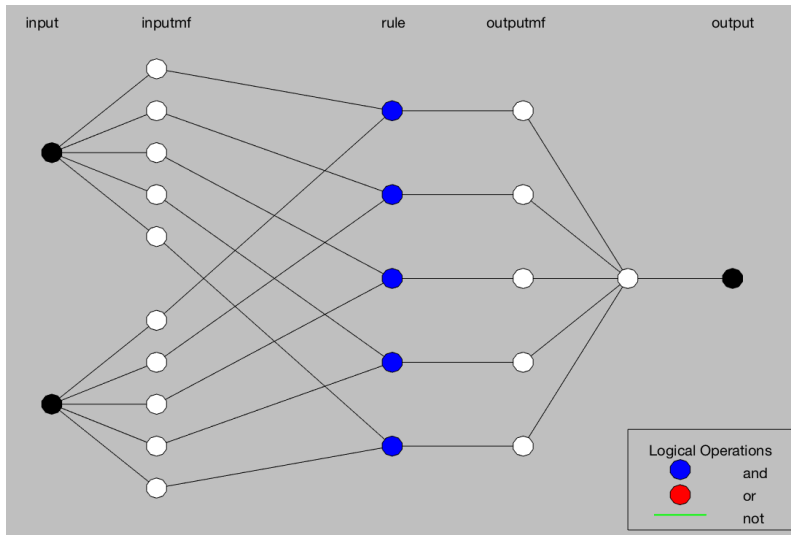
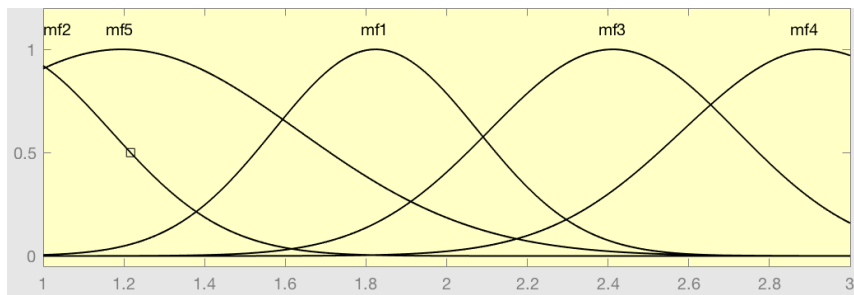
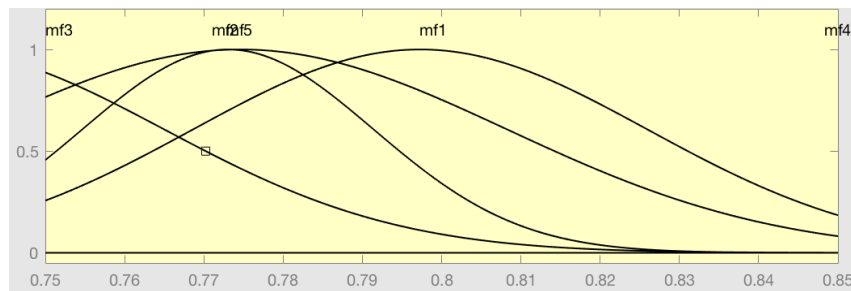


Figure 4.15: Matlab ANFIS Architecture.



(a) Input: exhaust flow velocity.



(b) Input: mounting height.

Figure 4.16: Membership Functions of inputs for basic ANFIS.

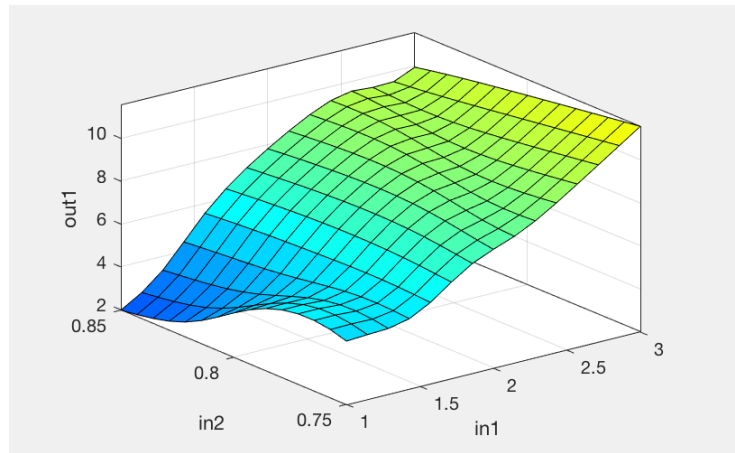


Figure 4.17: Relationship Between Two Inputs and One Output.

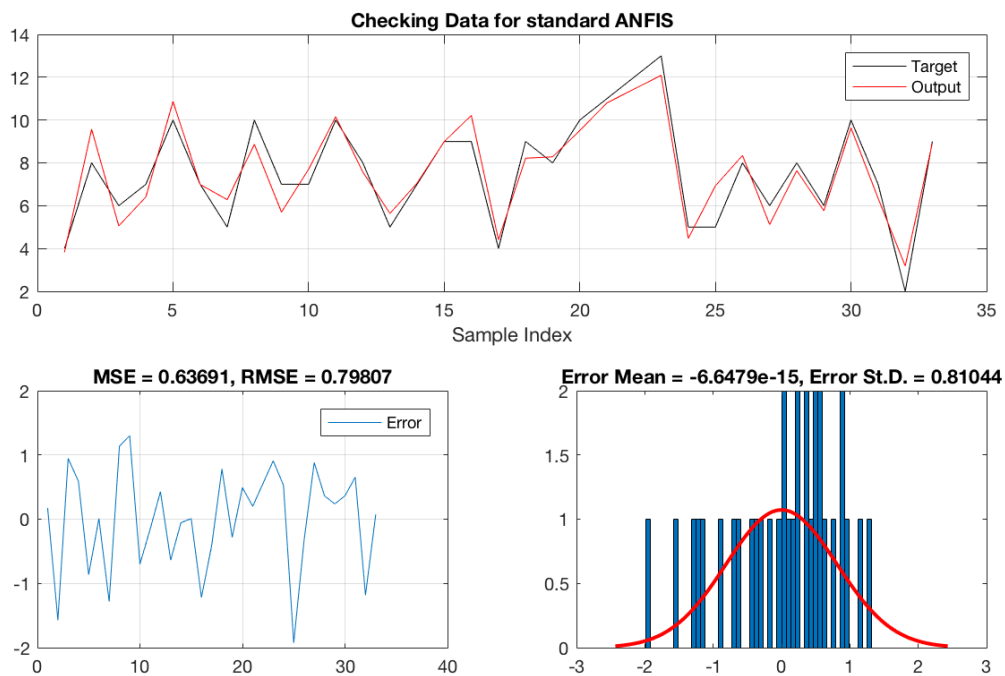
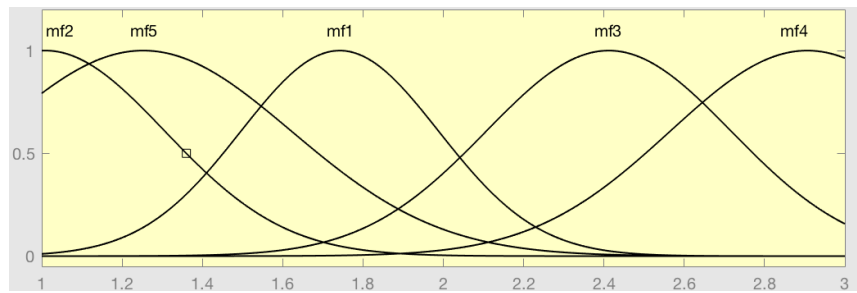


Figure 4.18: Checking Data and System Outputs for standard ANFIS.

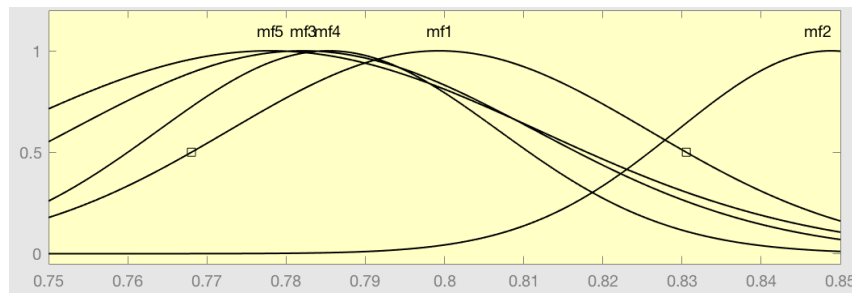
the root mean square error (RMSE) are 0.63691 and 0.79807, respectively. The mean value and standard deviation of all the errors are -6.6479×10^{-15} and 0.81044, respectively.

4.6.2 Results of ANFIS with PSO

The optimal membership functions ANFIS with PSO are shown in Figure 4.19a and Figure 4.19b. Input 33-row checking data to this ANFIS with PSO, the results are in Figure 4.20. It indicates that the mean squared error (MSE) and the root mean square error (RMSE) are 0.16638 and 0.4079, respectively. The mean value and standard deviation of all the errors are 0.021048 and 0.41367, respectively.



(a) Input: exhaust flow velocity.



(b) Input: mounting height.

Figure 4.19: Membership Functions of inputs for ANFIS with PSO.

Comparing the prediction results of the basic ANFIS controller and the ANFIS with PSO controller, the latter controller outputs obviously predict more checking data outputs correctly. The mean squared error of standard ANFIS is 0.63691, while the mean squared error of ANFIS with PSO is 0.16638. This means that, at the same situation (same training data and same number of iteration), the ANFIS with PSO controller performs better.



Figure 4.20: Checking Data and System Outputs for ANFIS with PSO.

Chapter 5

Conclusion and Future Works

5.1 Conclusion

In this thesis, a novel tornado-like-vortex generator (TLVG) was constructed and analyzed. The vertical pressure difference produced by the range hood and the horizontal shear force generated by the air jets from tubes in this TLVG are two main components of tornado-like vortex generation. A series of experiments and numerical simulations were designed to validate the TLVG's efficiency.

In the experiment, when the TLVG jet generator was switched on, the mist was drawn into the vortex column and exhausted through the range hood, while the mist dispersed around the mist maker when the TLVG jet generator was turned off. The numerical simulation results also showed that the TLVG offers a high-efficiency solution to enhance the performance of the exhaust. The region of negative pressure was extended to the source of the cooking fumes.

The numerical simulation and orthogonal experimental design were used to perform parametric analyses on jet velocity, range hood exhaust flow velocity, horizontal jet angle, mounting height, and distance between tubes to test the effects of the novel TLVG on the suction of cooking fumes. Those variables are sensitive to tornado-like vortex generation, and the associated results are summarized as follows:

The jet velocity, which is regulated by the DC fans in the generator of jets, directly affects the shear force intensity. Lower negative pressure is present in the cases of higher jet velocities, which will help concentrate and exhaust the mist. Jets with greater velocity, however, would consume more power.

The exhaust flow velocity only slightly affects the pressure around the cooking fumes' source, but if the value of the exhaust flow velocity is too high, the tornado-like vortex can not be produced.

The findings also show that the key factor affecting the performance of the TLVG is the horizontal jet angle. The suggested responses to the jet angle, mounting height, and tube distance factors are 0, 0.85 m, and 0.35 m, respectively.

This TLVG produces two tornado-like vortices at the same time, and their forms are not disturbed by one another. However, when two vortices are produced simultaneously, the effects of the novel TLVG on the suction of cooking fumes will decrease marginally compared to when they are produced separately.

The result also shows the feasibility of the TLVG with the side-suction range hood. This new TLVG is a high-efficiency indoor cooking fume suction solution. The findings in this paper provide a basis for the energy-saving direction of the range hood, which means that without high range hood capacity, the cooking fumes can be depleted.

In the end, the ANFIS controller is designed with the exhaust flow velocity and the mounting height as the inputs and the optimal jet velocity as the output. According to the results of the Matlab simulation, the controller can predict the optimal jet velocity of TLVG successfully. The results also reveal that the ANFIS-Swarm controller, which predicts more checking data outputs correctly under the same conditions, performs better than the traditional ANFIS controller.

5.2 Future Work

The design of the tubes of the novel TLVG including their shape, size, and arrangement is significant to the performance of the TLVG. To optimize the design, some quantitative tests should be conducted by numerical simulation methods.

- **Shape of Tubes:** The flow features of the jets may be related to the shape of the tube used in the TLVG device. Round tubes are easy to be bought or manufactured, but the rectangle tubes are more good looking in the industrial design. To find out the influence from the shape of tubes, cases of flow in a round tube and a rectangle tube need to be simulated in ANSYS FLUENT.
- **Length of Tubes:** The length of the tubes in this TLVG is restricted by many factors. Different types of range hoods and mounting heights require different lengths

of tubes. Besides, the heat of the stove will be reduced if the tube is too long and too close to the stove. Therefore, the numerical simulation needs to be done for different types of range hoods to find the optimal length of tubes in view of the efficiency of suction of cooking fumes and temperature distribution.

- **Structure of TLVG:** Fig. 5.1a is a schematic view of the first new version of the design of the top-suction range hood with a TLVG device. Only two tubes with the air channels are mounted on the back two corners below the range hood. However, it may be difficult to keep the tornado-like vortex in good shape. Fig. 5.1b is a schematic view of the second new version of the design of the top-suction range hood with a TLVG device. The tube with the air channel is mounted on the vertical central line of the backsplash. Two side panels are placed on both sides to concentrate the flow. To get enough power with only one tube, a small DC fan can not be chosen, which may bring a difficulty to the industrial design of this production. Fig. 5.1c is a schematic view of the third new version of the design of the side-suction range hood with a TLVG device. On the vertical central line of the backsplash, a shorter tube with an air channel is installed. Two longer tubes on both sides will move forward because of the position of the exhaust port of the side-suction range hood. Two side panels are placed on both sides to concentrate the flow. These designs need to be simulated and tested to compare their effectiveness.

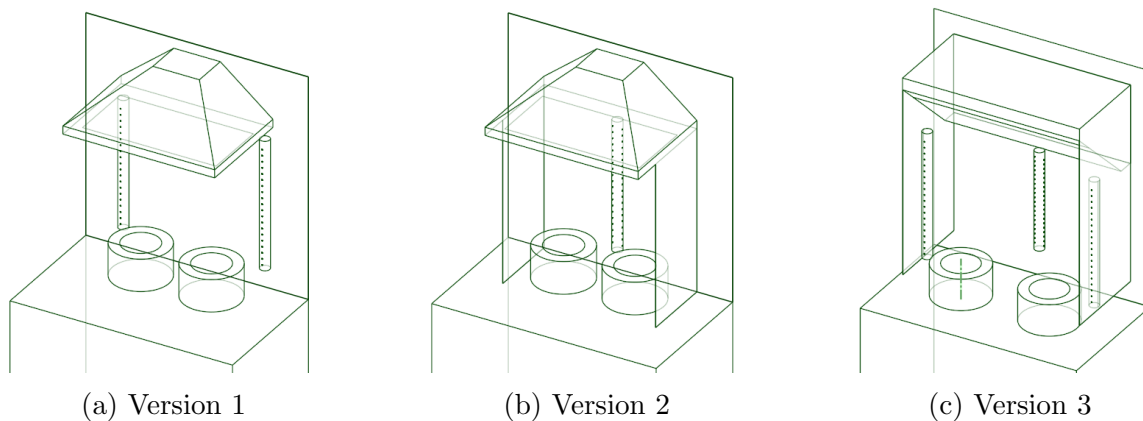


Figure 5.1: New structures of TLVG.

References

- [1] M. H. Ab Talib and I. Z. Mat Darus. Intelligent fuzzy logic with firefly algorithm and particle swarm optimization for semi-active suspension system using magnetorheological damper. *Journal of Vibration and Control*, 23(3):501–514, 2017.
- [2] J. Abanto and M. Reggio. Numerical investigation of the flow in a kitchen hood system. *Building and environment*, 41(3):288–296, 2006.
- [3] ANSYS 2020R1 Campus Solutions. Fluent.
- [4] G. Buonanno, L. Morawska, and L. Stabile. Particle emission factors during cooking activities. *Atmospheric Environment*, 43(20):3235–3242, 2009.
- [5] G. Buonanno, L. Stabile, L. Morawska, G. Giovinco, and X. Querol. Do air quality targets really represent safe limits for lung cancer risk? *Science of the Total Environment*, 580:74–82, 2017.
- [6] C. Cao, J. Gao, L. Wu, X. Ding, and X. Zhang. Ventilation improvement for reducing individual exposure to cooking-generated particles in chinese residential kitchen. *Indoor and Built Environment*, 26(2):226–237, 2017.
- [7] L. Casas, C. Tischer, C. Tiesler, I. Brüske, S. Koletzko, C.-P. Bauer, H.-E. Wichmann, A. Von Berg, D. Berdel, U. Krämer, et al. Association of gas cooking with children’s respiratory health: results from ginipus and lisaplus birth cohort studies. *Indoor air*, 22(6):476–482, 2012.
- [8] Fluent. Ansys fluent theory guide. *ANSYS Inc., USA*, 15317:724–746, 2011.
- [9] M. H. Golbon Haghighi, H. Saeidi Manesh, G. Zhang, and Y. Zhang. Pattern synthesis for the cylindrical polarimetric phased array radar (cpar). *Progress In Electromagnetics Research*, 66:87–98, 2018.

- [10] M. K. Heris. Evolutionary anfis training in matlab, 2015.
- [11] C. Hwang and K. Yoon. Methods for multiple attribute decision making. In *Multiple attribute decision making*, pages 58–191. Springer, 1981.
- [12] J. Jang. Anfis: adaptive-network-based fuzzy inference system. *IEEE transactions on systems, man, and cybernetics*, 23(3):665–685, 1993.
- [13] M. P. K. AnandaKumar. Efficient cancer classification using fast adaptive neuro-fuzzy inference system (fanfis) based on statistical techniques. *IJACSA) International Journal of Advanced Computer Science and Applications, Special Issue on Artificial Intelligence*, pages 132–137, 2011.
- [14] L. Kuai, F. L. Haan Jr, W. A. Gallus Jr, and P. P. Sarkar. Cfd simulations of the flow field of a laboratory-simulated tornado for parameter sensitivity studies and comparison with field measurements. *Wind and Structures*, 11(2):75–96, 2008.
- [15] M. Li, A. Vierkötter, T. Schikowski, A. Hüls, A. Ding, M. S. Matsui, B. Deng, C. Ma, A. Ren, J. Zhang, et al. Epidemiological evidence that indoor air pollution from cooking with solid fuels accelerates skin aging in chinese women. *Journal of dermatological science*, 79(2):148–154, 2015.
- [16] Y. Li and A. Delsante. Derivation of capture efficiency of kitchen range hoods in a confined space. *Building and Environment*, 31(5):461–468, 1996.
- [17] K. Lim and C. Lee. A numerical study on the characteristics of flow field, temperature and concentration distribution according to changing the shape of separation plate of kitchen hood system. *Energy and Buildings*, 40(2):175–184, 2008.
- [18] X. Liu, X. Wang, and G. Xi. Orthogonal design on range hood with air curtain and its effects on kitchen environment. *Journal of occupational and environmental hygiene*, 11(3):186–199, 2014.
- [19] A. Lohani, N. Goel, and K. Bhatia. Takagi sugeno fuzzy inference system for modeling stage–discharge relationship. *Journal of Hydrology*, 331(1-2):146–160, 2006.
- [20] T. Lundstedt, E. Seifert, L. Abramo, B. Thelin, Å. Nyström, J. Pettersen, and R. Bergman. Experimental design and optimization. *Chemometrics and intelligent laboratory systems*, 42(1-2):3–40, 1998.

- [21] P. Martínez, J. Ruiz, Í. Martín, and M. Lucas. Experimental study of an ultrasonic mist generator as an evaporative cooler. *Applied Thermal Engineering*, 181:116057, 2020.
- [22] F. R. Menter. Two-equation eddy-viscosity turbulence models for engineering applications. *AIAA journal*, 32(8):1598–1605, 1994.
- [23] E. Mills and D. Sartor. Energy use and savings potential for laboratory fume hoods. *Energy*, 30(10):1859–1864, 2005.
- [24] M. Pinelli and A. Suman. A numerical method for the efficient design of free opening hoods in industrial and domestic applications. *Energy*, 74:484–493, 2014.
- [25] N. M. Razali, J. Geraghty, et al. Genetic algorithm performance with different selection strategies in solving tsp. In *Proceedings of the world congress on engineering*, volume 2, pages 1–6. International Association of Engineers Hong Kong, 2011.
- [26] J. Ren and Y. Xiong. An optimised method of weighting combination in multi-index comprehensive evaluation. *International Journal of Applied Decision Sciences*, 3(1):34–52, 2010.
- [27] R. Rotunno. The fluid dynamics of tornadoes. *Annual review of fluid mechanics*, 45, 2013.
- [28] L. Ruijiang, Z. Yewang, W. Chongwei, and T. Jian. Study on the design and analysis methods of orthogonal experiment [j]. *Experimental Technology and Management*, 9:52–55, 2010.
- [29] J. Ruiz Ramírez, P. Martínez Martínez, Í. Martín Melero, and L. Miralles Manuel. Numerical characterization of an ultrasonic mist generator as an evaporative cooler. *Energies*, 13(11):2971, 2020.
- [30] J. J. Schauer, M. J. Kleeman, G. R. Cass, and B. R. Simoneit. Measurement of emissions from air pollution sources. 4. c1- c27 organic compounds from cooking with seed oils. *Environmental Science & Technology*, 36(4):567–575, 2002.
- [31] J. Soto, P. Melin, and O. Castillo. Optimization of interval type-2 fuzzy integrators in ensembles of anfis models for prediction of the mackey-glass time series. In *2014 IEEE Conference on Norbert Wiener in the 21st Century (21CW)*, pages 1–8. IEEE, 2014.

- [32] M. Turki, S. Bouzaida, A. Sakly, and F. M'Sahli. Adaptive control of nonlinear system using neuro-fuzzy learning by pso algorithm. In *2012 16th IEEE Mediterranean Electrotechnical Conference*, pages 519–523. IEEE, 2012.
- [33] H. Xiang, B. Lei, Z. Li, K. Zhao, Q. Lv, Q. Zhang, and Y. Geng. Analysis of parameter sensitivity of induction coil launcher based on orthogonal experimental method. *IEEE Transactions on Plasma Science*, 43(5):1198–1202, 2015.
- [34] X. Yang. *Nature-inspired metaheuristic algorithms*. Luniver press, 2010.
- [35] F. Yik and P. Au. Flow rate and capture efficiency of domestic kitchen exhaust hoods for chinese households. *Int. J. Arch. Sci*, 3:125–134, 2002.
- [36] P. Zhang, G. Y. Ouyang, and J. M. Lv. Orthogonal experimental design applied in analyzing factors influencing on heat transfer performance of engine cylinder head. volume 383, pages 4783–4786. Trans Tech Publ, 2012.
- [37] J. Zhu, D. A. Chew, S. Lv, and W. Wu. Optimization method for building envelope design to minimize carbon emissions of building operational energy consumption using orthogonal experimental design (oed). *Habitat International*, 37:148–154, 2013.

APPENDICES

Appendix A

Orthogonal Table

Orthogonal experimental design (OED) is created by Taguchi in 1950s. It is a design method that studies multiple factors and levels, and it finds the optimal level combination only upon part of the experiments.

The orthogonal table is the foundation of the orthogonal experimental design, which forms as follow:

$$L_n(k^m)$$

where the L is the symbol of the orthogonal table; n is the number of schemes (rows) in the orthogonal table; k is the number of levels for every factor; m is the number of factors (columns) in the orthogonal table;

The orthogonal experimental design may use existing orthogonal table, and it can also use mathematical model to create an orthogonal table. The orthogonal table primarily uses the abstract algebra theory, and there are several existing standard orthogonal tables, such as $L_4(2^3)$, $L_8(2^7)$, $L_9(3^4)$, $L_{16}(4^5)$, $L_{18}(3^5)$, etc.

Let's take $L_9(3^4)$ as an example. 27 intersection points of the cube, which represent the full experiment's 27 experimental points, and 9 experimental points of OED are shown in Fig. A.1 [37]. For each plane containing 9 intersection points, there are happen to be 3 experimental points in the orthogonal table. There are 6 lines on each plane, and there is happen to be 1 experimental point in the orthogonal table for each line. Therefore, among these intersection points, 9 experimental points chosen by the orthogonal table are distributed uniformly in the three-dimensional space.

There are two key properties of the $L_9(3^4)$ orthogonal table (Table A.1):

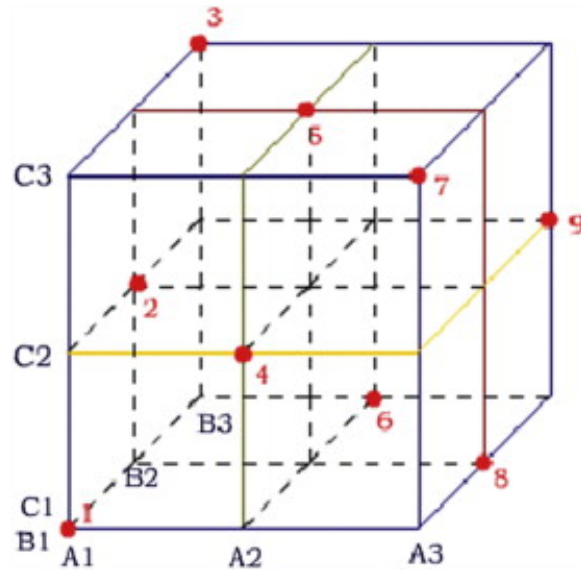


Figure A.1: Nine experimental points in the three-dimensional space.

Table A.1: $L_9(3^4)$ orthogonal table.

| Exp. No. | Factor 1 | Factor 2 | Factor 3 | Factor 4 |
|----------|----------|----------|----------|----------|
| 1 | level A | level A | level A | level A |
| 2 | level A | level B | level B | level B |
| 3 | level A | level C | level C | level C |
| 4 | level B | level A | level B | level C |
| 5 | level B | level B | level C | level A |
| 6 | level B | level C | level A | level B |
| 7 | level C | level A | level C | level B |
| 8 | level C | level B | level A | level C |
| 9 | level C | level C | level B | level A |

- The number of occurrences of different levels in each column should be the same. For example, the levels in each column are A, B and C, and each of them appears 3 times;

- The number of occurrences of any two factors with different level combinations should be the same. For example, there are 9 level combinations: (A, A), (A, B), (A, C), (B, A), (B, B), (B, C), (C, A), (C, B) and (C, C). Each of these combinations appears once.

The standard $L_{18}(3^5)$ orthogonal table used in this thesis is list in Table A.2.

Table A.2: $L_{18}(3^5)$ orthogonal table.

| Exp. No. | Factor 1 | Factor 2 | Factor 3 | Factor 4 | Factor 5 |
|----------|----------|----------|----------|----------|----------|
| 1 | level A | level A | level A | level A | level A |
| 2 | level A | level B | level B | level B | level B |
| 3 | level A | level C | level C | level C | level C |
| 4 | level B | level A | level A | level B | level B |
| 5 | level B | level B | level B | level C | level C |
| 6 | level B | level C | level C | level A | level A |
| 7 | level C | level A | level B | level A | level C |
| 8 | level C | level B | level C | level B | level A |
| 9 | level C | level C | level A | level C | level B |
| 10 | level A | level A | level C | level C | level B |
| 11 | level A | level B | level A | level A | level C |
| 12 | level A | level C | level B | level B | level A |
| 13 | level B | level A | level B | level C | level A |
| 14 | level B | level B | level C | level A | level B |
| 15 | level B | level C | level A | level B | level C |
| 16 | level C | level A | level C | level B | level C |
| 17 | level C | level B | level A | level C | level A |
| 18 | level C | level C | level B | level A | level B |

Appendix B

Matlab Code

```
%% main.m %%
% create initial fis with 5 clusters
fis=CreateInitialFIS(trn,5);
% training fis using PSO
fisPSO=TrainAnfisUsingPSO(fis,trn);
% plot
TrainOutputs=evalfis(trn(:,1:2),fis);
TrainOutputsPSO=evalfis(trn(:,1:2),fisPSO);
PlotResults(trn(:,3),TrainOutputs,'Checking Data for standard ANFIS');
hold on;
PlotResults(trn(:,3),TrainOutputsPSO,'Checking Data for ANFIS with PSO');
```

```
%% CreateInitialFIS.m %%
function fis=CreateInitialFIS(data,nCluster)

    if ~exist('nCluster','var')
        nCluster='auto';
    end

    x = data(:,1:2); % inputs
    t = data(:,3); % output

    fcm_U=2;
```

```

fcm_MaxIter=1000;
fcm_MinImp=1e-5;
fcm_Display=false;

opt = genfisOptions('FCMClustering');
opt.FISType = 'sugeno';
opt.NumClusters = nCluster;
opt.Exponent = fcm_U;
opt.MaxNumIteration = fcm_MaxIter;
opt.MinImprovement = fcm_MinImp;
opt.Verbose = fcm_Display;
fis = genfis(x,t,opt);

end

%%% TrainAnfisUsingPSO.m %%%
function bestfis=TrainAnfisUsingPSO(fis,data)

%% Problem Definition

p0=GetFISParams(fis);

Problem.CostFunction=@(x) TrainFISCost(x,fis,data);
Problem.nVar=numel(p0);
Problem.VarMin=-25;
Problem.VarMax=25;

%% PSO Params
Params.MaxIt=1000;
Params.nPop=50;

%% Run PSO
results=RunPSO(Problem,Params);

%% Get Results

p=results.BestSol.Position.*p0;

```

```

    bestfis=SetFISParams(fis,p);

end

function results=RunPSO(Problem,Params)

    disp('Starting PSO ...');

    %% Problem Definition

    CostFunction=Problem.CostFunction;          % Cost Function

    nVar=Problem.nVar;                          % Number of Decision Variables

    VarSize=[1 nVar];                          % Size of Decision Variables Matrix

    VarMin=Problem.VarMin;                      % Lower Bound of Variables
    VarMax=Problem.VarMax;                      % Upper Bound of Variables

    %% PSO Parameters

    MaxIt=Params.MaxIt;                        % Maximum Number of Iterations

    nPop=Params.nPop;                          % Population Size (Swarm Size)

    w=1;                                        % Inertia Weight
    wdamp=0.99;                                % Inertia Weight Damping Ratio
    c1=1;                                       % Personal Learning Coefficient
    c2=2;                                       % Global Learning Coefficient

    % Velocity Limits
    VelMax=0.1*(VarMax-VarMin);
    VelMin=-VelMax;

    %% Initialization

    empty_particle.Position=[];
    empty_particle.Cost=[];

```

```

empty_particle.Velocity=[];
empty_particle.Best.Position=[];
empty_particle.Best.Cost=[];

particle= repmat(empty_particle,nPop,1);

BestSol.Cost=inf;

for i=1:nPop

    % Initialize Position
    if i>1
        particle(i).Position=unifrnd(VarMin,VarMax,VarSize);
    else
        particle(i).Position=ones(VarSize);
    end

    % Initialize Velocity
    particle(i).Velocity=zeros(VarSize);

    % Evaluation
    particle(i).Cost=CostFunction(particle(i).Position);

    % Update Personal Best
    particle(i).Best.Position=particle(i).Position;
    particle(i).Best.Cost=particle(i).Cost;

    % Update Global Best
    if particle(i).Best.Cost<BestSol.Cost

        BestSol=particle(i).Best;

    end

end

BestCost=zeros(MaxIt,1);

```



```

%% PSO Main Loop

for it=1:MaxIt

    for i=1:nPop

        % Update Velocity
        particle(i).Velocity = w*particle(i).Velocity ...
            +c1*rand(VarSize).*(particle(i).Best.Position-particle(i).Position) ...
            +c2*rand(VarSize).*(BestSol.Position-particle(i).Position);

        % Apply Velocity Limits
        particle(i).Velocity = max(particle(i).Velocity,VelMin);
        particle(i).Velocity = min(particle(i).Velocity,VelMax);

        % Update Position
        particle(i).Position = particle(i).Position + particle(i).Velocity;

        % Velocity Mirror Effect
        IsOutside=(particle(i).Position<VarMin | particle(i).Position>VarMax);
        particle(i).Velocity(IsOutside)=-particle(i).Velocity(IsOutside);

        % Apply Position Limits
        particle(i).Position = max(particle(i).Position,VarMin);
        particle(i).Position = min(particle(i).Position,VarMax);

        % Evaluation
        particle(i).Cost = CostFunction(particle(i).Position);

        % Update Personal Best
        if particle(i).Cost<particle(i).Best.Cost

            particle(i).Best.Position=particle(i).Position;
            particle(i).Best.Cost=particle(i).Cost;

            % Update Global Best
            if particle(i).Best.Cost<BestSol.Cost

```

```

        BestSol=particle(i).Best;

    end

end

end

BestCost(it)=BestSol.Cost;

disp(['Iteration ' num2str(it) ': Best Cost = ' num2str(BestCost(it))]);

w=w*wdamp;

end

disp('End of PSO. ');
disp(' ');

%% Results

results.BestSol=BestSol;
results.BestCost=BestCost;

end

%%%% GetFISParams.m %%%%
function p=GetFISParams(fis)

p=[];

nInput=numel(fis.input);
for i=1:nInput
    nMF=numel(fis.input(i).mf);
    for j=1:nMF
        p=[p fis.input(i).mf(j).params];
    end
end
end

```

```

nOutput=numel(fis.output);
for i=1:nOutput
    nMF=numel(fis.output(i).mf);
    for j=1:nMF
        p=[p fis.output(i).mf(j).params];
    end
end
end

end

%%%% SetFISParams.m %%%%
function fis=SetFISParams(fis,p)

nInput=numel(fis.input);
for i=1:nInput
    nMF=numel(fis.input(i).mf);
    for j=1:nMF
        k=numel(fis.input(i).mf(j).params);
        fis.input(i).mf(j).params=p(1:k);
        p(1:k)=[];
    end
end

nOutput=numel(fis.output);
for i=1:nOutput
    nMF=numel(fis.output(i).mf);
    for j=1:nMF
        k=numel(fis.output(i).mf(j).params);
        fis.output(i).mf(j).params=p(1:k);
        p(1:k)=[];
    end
end

end
end

```

```

%% TrainFISCost.m
function [z, out]=TrainFISCost(x,fis,data)

    MinAbs=1e-5;
    if any(abs(x)<MinAbs)
        S=(abs(x)<MinAbs);
        x(S)=MinAbs.*sign(x(S));
    end

    p0=GetFISParams(fis);

    p=x.*p0;

    fis=SetFISParams(fis,p);

    x = data(:,1:2);
    t = data(:,3);
    y=evalfis(x,fis);

    e=t-y;

    MSE=mean(e(:).^2);
    RMSE=sqrt(MSE);

    z=RMSE;

    out.fis=fis;
    out.MSE=MSE;
    out.RMSE=RMSE;

end

%% PlotResults.m
function PlotResults(Targets, Outputs, Name)

    figure;

```

```

Errors=Targets-Outputs;

MSE=mean(Errors.^2);
RMSE=sqrt(MSE);

error_mean=mean(Errors);
error_std=std(Errors);

subplot(2,2,[1 2]);
plot(Targets,'k');
hold on;
plot(Outputs,'r');
legend('Target','Output');
title(Name);
xlabel('Sample Index');
grid on;

subplot(2,2,3);
plot(Errors);
legend('Error');
title(['MSE = ' num2str(MSE) ', RMSE = ' num2str(RMSE)]);
grid on;

subplot(2,2,4);
histfit(Errors, 50);
title(['Error Mean = ' num2str(error_mean) ', Error St.D. = ' num2str(error_std)]);

end

```